



Article

One-Step Dry Coating of Hybrid ZnO–WO₃ Nanosheet Photoanodes for Photoelectrochemical Water Splitting with Composition-Dependent Performance

Muhammad Shehroze Malik ¹, Deepto Roy ¹, Doo-Man Chun ^{1,*} and A. G. Abd-Elrahim ^{1,2}

¹ School of Mechanical Engineering, University of Ulsan, Ulsan 44610, Republic of Korea; shehrozemalik80@gmail.com (M.S.M.); deepto43.me@gmail.com (D.R.); ahmed_galal@aun.edu.eg (A.G.A.-E.)
² Physics Department, Faculty of Science, Assiut University, Assiut 71516, Egypt
* Correspondence: dmchun@ulsan.ac.kr

Abstract: In this study, the potential of zinc oxide (ZnO), tungsten oxide (WO₃), and their composites (ZnO–WO₃) as photoanodes for photoelectrochemical (PEC) water splitting was investigated. ZnO–WO₃ nanocomposites (NCs) were deposited on fluorine-doped tin oxide substrates at room temperature using a one-step dry coating process, the nanoparticle deposition system, with no post-processes. Different compositions of ZnO–WO₃ NCs were optimized to enhance the kinetics of the PEC water-splitting reaction. Surface morphology analysis revealed the transformation of microsized particle nanosheets (NS) powder into nanosized particle nanosheets (NS) across all photoanodes. The optical characteristics of ZnO–WO₃ photoanodes were scrutinized using diffuse reflectance and photoluminescence emission spectroscopy. Of all the hybrid photoanodes tested, the photoanode containing 10 wt.% WO₃ exhibited the lowest bandgap of 3.20 eV and the lowest emission intensity, indicating an enhanced separation of photogenerated carriers and solar energy capture. The photoelectrochemical results showed a 10% increase in the photocurrent with increasing WO₃ content in ZnO–WO₃ NCs, which is attributed to improved charge transfer kinetics and carrier segregation. The maximum photocurrent for a NC, i.e., 10 wt.% WO₃, was recorded at 0.133 mA·cm^{−2} at 1.23V vs. a reversible hydrogen electrode (RHE). The observed improvement in photocurrent was nearly 22 times higher than pure WO₃ nanosheets and 7.3 times more than that of pure ZnO nanosheets, indicating the composition-dependence of PEC performance, where the synergy requirement strongly relies on utilizing the optimal ZnO–WO₃ ratio in the hybrid NCs.



Citation: Malik, M.S.; Roy, D.; Chun, D.-M.; Abd-Elrahim, A.G. One-Step Dry Coating of Hybrid ZnO–WO₃ Nanosheet Photoanodes for Photoelectrochemical Water Splitting with Composition-Dependent Performance. *Micromachines* **2023**, *14*, 2189. <https://doi.org/10.3390/mi14122189>

Academic Editor: Aiqun Liu

Received: 6 November 2023

Revised: 22 November 2023

Accepted: 28 November 2023

Published: 30 November 2023



Copyright: © 2023 by the authors. Licensee MDPI, Basel, Switzerland. This article is an open access article distributed under the terms and conditions of the Creative Commons Attribution (CC BY) license (<https://creativecommons.org/licenses/by/4.0/>).

Keywords: ZnO–WO₃ hybrid photoanodes; charge transfer kinetics; photoelectrochemical water splitting; nanoparticle deposition system (NPDS); nanosheets; nanocomposites; bandgap optimization

1. Introduction

Photoelectrochemical (PEC) water splitting is a promising technique that involves the direct conversion of sunlight and water into electricity and hydrogen. This method is notably regarded as a simple, economical, and direct energy conversion route toward a sustainable, clean, and green society [1–3]. Presently, a major source of energy (80%) on earth comes from fossil fuels, such as oil, natural gas, and coal, which are rapidly depleting and unsustainable, resulting in a drastic change in climate through global warming and other forms of pollution. Therefore, it has become necessary to shift toward green, renewable, and environmentally friendly energy sources such as solar, wind, and geothermal energy to meet global energy demand while minimizing environmental impact and cost [4,5].

Significant efforts have been made to advance metal oxide photoanodes (ZnO, TiO₂, WO₃, Fe₂O₃, and BiVO₄) [3,6–11], particularly in heterostructured electrode forms, to improve system performance. Meeting the specifications of an efficient PEC water-splitting system using a single semiconductor presents challenges [12,13]. Essentially, the overall performance is based on four key steps: (a) absorption of light and generation of charge

carriers; (b) separation of charges; (c) efficient transportation of charges; and (d) extraction of the charge carriers [14]. Therefore, this study focuses on developing heterojunction-based nanocomposites (NCs) for photoanodes, aiming to enhance practical applications in PEC systems. We integrated two semiconductors, ZnO (bandgap = 3.35 eV) [15] and WO₃ (bandgap = 2.8 eV) [16], using a nanoparticle deposition system (NPDS) [15,17]. ZnO, widely used in photovoltaics applications, offers various advantages like cost-effectiveness, favorable bandgap, high electron mobility (bulk mobility: 200 cm²·V⁻¹·s⁻¹), long life time of minority carriers, and good separation of photogenerated carriers [18]. However, its limited light absorption in the visible-infrared spectrum due to its wide bandgap (~3.35 eV) [19] necessitates a solution. To address ZnO's light absorption limitation, we combined it with a narrow-bandgap semiconductor, tungsten trioxide (WO₃). This strategic incorporation aims to expand ZnO's light absorption range. Tungsten trioxide possesses exceptional properties such as high electron mobility, photostability, and a long hole-diffusion length (~150 nm) [20], making it a good candidate to broaden ZnO's visible absorbance range. This combination forms ZnO/WO₃ heterostructures, promising to extend the spectrum of light absorption and enhance the performance of photoelectrochemical applications.

So far, vast efforts have been concentrated on the preparation of hybrid heterostructured photoanodes to achieve a lower bandgap, efficient segregation of photogenerated electron-hole pairs due to appropriate band alignment, and enhanced photoresponse current. D. Barreca et al. [6] prepared ZnO–WO₃ nano-heterostructures using a multistep vapor phase process. First, ZnO samples were prepared within a reservoir using a 3 h thermal treatment at 550 °C. Second, ZnO was mixed with the WO₃ layers under optimized conditions: pressure = 0.3 M bar and RF power = 20 W for 3 h. The obtained ZnO–WO₃ composites achieved a 0.055 mA·cm⁻² photocurrent at 0.8 V vs. Ag/AgCl in 0.5 M Na₂SO₄. Y. Xu et al. [21] prepared ZnO thin films by hydrothermal synthesis at 95 °C for 4 h. WO₃ was then deposited on the prepared ZnO samples using magnetron sputtering at 1 Pa ambient air pressure and 65 W RF sputtering power. The ZnO–WO₃ composites obtained in their research achieved a photocurrent of 0.353 mA/cm² at 0.3 V vs. Ag/AgCl in a 0.5 M Na₂SO₄ solution. J. Ji et al. [22] prepared WO₃–BiVO₄–ZnO using different steps. Tungstic acid and a polyvinyl alcohol solution were dissolved to produce a 0.12 M WO₃ precursor solution. Then they annealed the solution for 1 h at 500 °C. The same procedure was repeated for BiVO₄ on the WO₃ film to obtain the WO₃/BiVO₄ films. Finally, a ZnO solution was prepared and deposited onto the WO₃/BiVO₄ films using spin coating. In this study, the obtained WO₃–BiVO₄–ZnO composite at 1.23 V vs. the RHE exhibited a photocurrent of 0.190 mA/cm² in a 0.5 M Na₂SO₄ electrolyte.

The studies described above focusing on the combination of WO₃ and ZnO to produce heterostructure photoanodes show good performance in neutral electrolytes toward PEC water splitting. However, these synthesis techniques can only be used for small substrates and are limited to research and development, not commercial use. This is the case for several reasons: (a) the considerable time required for fabricating small-sized electrodes through multiple steps to achieve the required nanosized powder, followed by its deposition onto substrates; (b) the use of dangerous reactant chemicals that produce useless toxic secondary products as waste; and (c) the difficulty in scaling up for commercial applications because of the time-consuming above techniques. In comparison, the NPDS has distinct features such as (a) one-step dry coating using the vacuum kinetic spray process at room temperature; (b) no hazardous chemicals or waste; (c) facile production of sizable electrodes for mass manufacturing in a convenient manner; (d) binder-free; and (e) no additional drying process [23,24].

In the present study, the NPDS was used to fabricate ZnO–WO₃ hybrid photoanodes at different WO₃ contents (5, 10, 15, and 20 wt.%) on fluorine-doped tin oxide (FTO) substrates. The deposition process involved the localized and spontaneous fragmentation of microsized powder into nanosized thin films at room temperature and low vacuum conditions. The modified working electrodes with ZnO–WO₃ hybrid NCs were utilized as photoanodes for the PEC water-splitting process in a neutral medium. Our study

systematically explored the impact of varying tungsten oxide (WO_3) weight ratios on charge transfer kinetics, bandgap engineering, and the efficiency of photogenerated charge carrier separation. The present study research outcomes demonstrate the composition-dependent PEC performance of ZnO-WO_3 hybrid photoanodes, which need to be optimized to improve the overall performance for real-life applications.

2. Experimental

2.1. Material Details

Microsized ZnO powder ($<5 \mu\text{m}$ particle size, 99.9%, CAS # 1314-13-2, Sigma-Aldrich, St. Louis, MO, USA) and WO_3 microsized powder ($\leq 25 \mu\text{m}$, $\geq 99\%$ trace metals basis, CAS # 1314-35-8, Sigma-Aldrich, St. Louis, MO, USA) were used to fabricate ZnO-WO_3 nanocomposites on a 2.3 mm thick FTO ($100 \times 100 \text{ mm}^2$, surface resistivity = $7 \Omega/\text{sq}$, Sigma-Aldrich, St. Louis, MO, USA). A 0.5 M Na_2SO_4 solution electrolyte was used as an agent with a pH of 6.8 (CAS# 7757-83-7, Duksan, Ansan-si, Republic of Korea) for the investigation of PEC water splitting.

2.2. Dry Coating of ZnO-WO_3 Thin Films by the NPDS

Nanostructured ZnO-WO_3 thin films with varying WO_3 (5%, 10%, 15%, and 20%) were deposited on the FTO by a one-step vacuum kinetic spray process, the NPDS. The NPDS is composed of an air compressor that supplies high pressure, a cylindrical piston known as a powder feeder, a vacuum pump, a nozzle, a controller, and a pressure chamber. The pressure was adjusted through the controller, and the microsized dry powder was mixed using a ball mill filled with a powder feeder that moved the powder to the powder chamber, where a rotating brush drives the powder and high-speed air pressure from the air compressor enters the nozzle. The powder was sprayed onto the substrate using a converging-diverging nozzle at room temperature. The impact of high-speed powder particles and the incident angle of the FTO substrate fractured the microsized powder into a nanosize range [25]. The conditions for deposition were set to a 3 mm standoff distance. The air compressor pressure was 3 bar, and the chamber pressure was 0.50 bar. More details are shown in Figure 1. The fabrication time for $40 \times 10 \text{ mm}^2$ samples using simple scanning and vacuum was less than 30 min. After deposition, there was no post-processing.

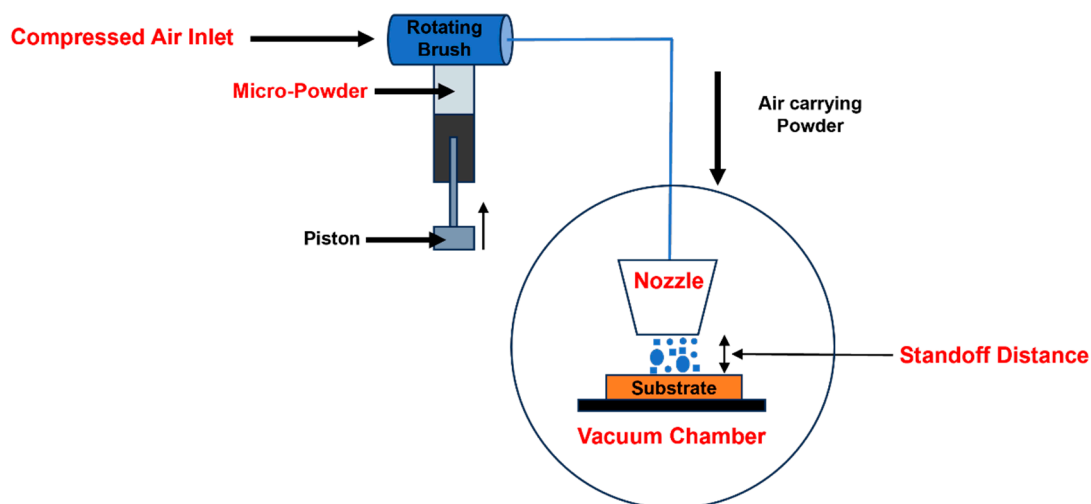


Figure 1. Deposition of nanostructured zinc-oxide-tungsten oxide hybrid photoanodes using the nanoparticle deposition system.

2.3. Photoelectrochemical Water Splitting Characteristics

An electrochemical workstation (Model: C350, Wuhan Corr-Test Instruments Corp. Ltd., Wuhan, China) and a solar simulator (Model: 10500, ABET Technologies, Milford, CT, USA) with a 150 W Xe Arc Lamp as a light source were used in a three-electrode

setup to evaluate ZnO–WO₃ NCs in a 0.5 M Na₂SO₄ electrolytic solution. ZnO/FTO, WO₃/FTO, and ZnO/WO₃/FTO hybrid photoanodes with varying WO₃ content were used as the working electrodes. The counter electrode was platinum (Pt) with a mesh area of 1 × 1 cm², and the reference electrode was Hg/HgO in a 0.5 M Na₂SO₄ electrolyte solution. Linear sweep voltammetry (LSV) profiles were examined within the potential range of −0.499–1.001 vs. Hg/HgO at a scan rate of 10 mV·s^{−1}. The potential range vs. the reference electrode was then converted to the reversible hydrogen electrode (RHE) scale using Equation (1) [26].

$$E_{\text{RHE}} = E_{\text{Hg/HgO}}^{\text{O}} + E_{\text{Hg/HgO}} + 0.059 \times \text{pH} \quad (1)$$

where $E_{\text{Hg/HgO}}^{\text{O}}$ is the reference electrode potential vs. SHE (0.059), the pH is 6.8, and $E_{\text{Hg/HgO}}$ is the applied potential. Therefore, the LSV curves were converted to 0–1.5 vs. the RHE. The charge transfer resistance (R_{ct}) was evaluated by Nyquist plot under illumination with an AC frequency of 10 mV and a frequency range of 1 MHz–0.001 Hz. Photocurrent stability was assessed through a series of chronoamperometric (CA) measurements at a DC potential of 1.23 V vs. the RHE over five full cycles under both dark and light conditions. Mott–Schottky (M–S) plots were created in the dark using electrochemical impedance spectroscopy with an AC signal of 10 mV ranging from −1–0 V vs. Hg/HgO at a frequency of 1 kHz.

2.4. Material Characterization

The surface morphology was examined using scanning electron microscopy (SEM, Model: S-4800, Hitachi, Chiyoda City, Tokyo, Japan) of micropowder and nanocomposite thin films. The structures of ZnO, WO₃, and hybrid photoanodes thin films and powders were examined using X-ray diffraction (XRD, Smart Lab, Shibuya-ku, Tokyo, Japan) with the X-ray wavelength Cu K-alpha from a diffraction angle of 10° to 90°. The Raman spectra for micropowder and nanostructured thin films were examined using a 1 mW laser source with a 532 nm excitation wavelength (Model: Alpha 300R, WITec, Ulm, Germany) in the range of 200–1200 cm^{−1}. Furthermore, the bonding states within ZnO, WO₃, and ZnO with varying WO₃ content photoanodes binding energies ranging from 0 to 1200 eV were examined using a source K-alpha X-ray photoelectron spectrometer. Photoluminescence (PL) emissions were recorded using a fluorescence spectrometer (Cary Eclipse, Varian, Santa Clara, CA, USA) in a range of 350–600 nm wavelength. Furthermore, the optical diffuse reflectance (DRS) of nanostructured ZnO, WO₃, and ZnO–WO₃ hybrid photoanodes was measured using a UV–Vis–NIR spectrophotometer (Cary 5000, Agilent, Santa Clara, CA, USA) in the wavelength range of 300–699 nm.

3. Results and Discussion

3.1. XRD Analysis

The crystalline structures of ZnO, WO₃, and ZnO–WO₃ mixed micron particle powders at various concentrations of 5, 10, 15, and 20 wt.% WO₃ were examined using XRD patterns (Figure 2a). The XRD pattern of ZnO shows characteristic diffraction peaks at 31.16°, 33.82°, 35.64°, 46.96°, 56.02°, 62.3°, 65.82°, 67.42°, and 68.56°. These peaks correspond to (1 0 0), (0 0 2), (1 0 1), (1 0 2), (1 1 0), (1 0 3), (2 0 0), (1 1 2), and (2 0 1) hexagonal ZnO phase crystalline planes (space group: P6_{3mc}, 01–086–8198), respectively [27]. The microsized WO₃ powder exhibited three main diffraction peaks at 22.56°, 23.04°, and 23.82°, corresponding to (0 0 2), (0 2 0), and (2 0 0) monoclinic WO₃ phase crystalline planes (space group: P2_{1/n}, 00–043–1035), respectively [28]. The composite powders, composed of various proportions of ZnO with WO₃ content ranging from 5% to 20%, displayed peaks corresponding to both ZnO and WO₃. This observation suggests the coexistence of hexagonal ZnO and monoclinic WO₃ in the composite materials. Additionally, there is no new hybrid structural phase because of the predeposition grinding achieved through the ball milling process [29].

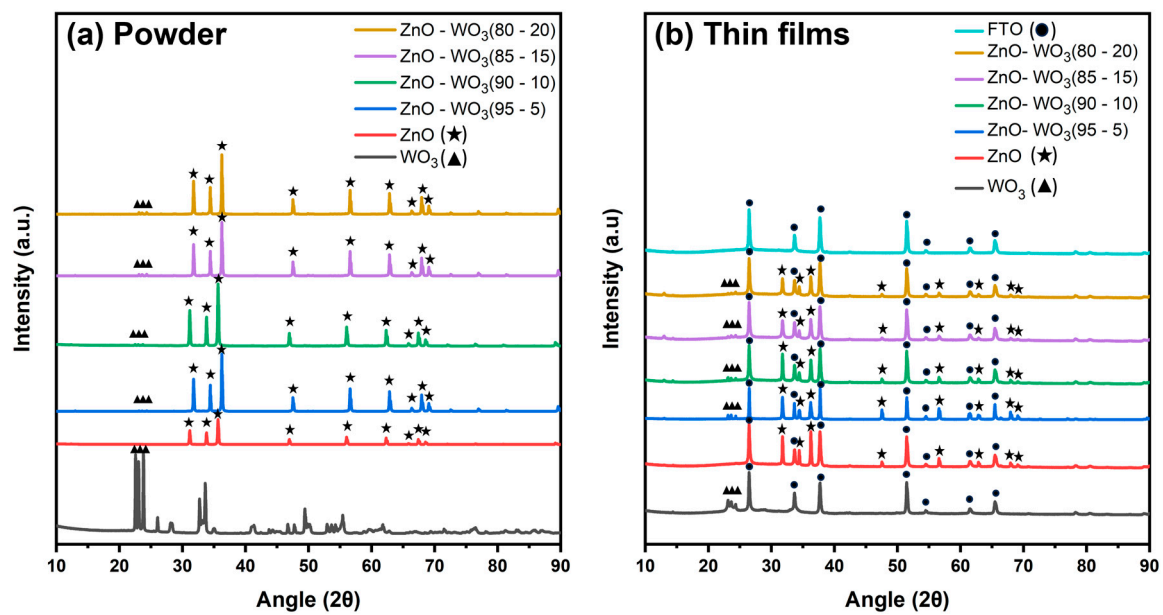


Figure 2. X-ray diffraction patterns of ZnO–WO₃ in powder form (a) and ZnO–WO₃ coated on a fluorine-doped tin oxide substrate (b).

Figure 2b shows the XRD patterns of the bare FTO substrate and nanostructured thin films of ZnO, WO₃, and ZnO–WO₃ hybrid NCs at different WO₃ contents (5, 10, 15, and 20 wt.%) on FTO. The XRD pattern of FTO shows several peaks at 26.48°, 33.66°, 37.72°, 54.5°, 61.5°, and 65.46°. The XRD pattern of the nanosized pure ZnO thin film shows peaks at 31.78°, 34.42°, 36.36°, 47.56°, 56.58°, 62.86°, 67.94°, and 69.08°. For the WO₃ thin film, only major peaks are visible at 23.12°, 23.64°, and 24.38° because of its low content in the nanocomposites (NCs). It is observed that the thin film peak positions have shifted a little compared to the powder peak positions. This is because of fracturing, shattering, and random ordering of the particles during deposition [30]. Overall, the XRD patterns of the ZnO, WO₃, and ZnO–WO₃ NC thin films show relatively smaller peak intensities than those of the corresponding powder. This behavior is attributed to the polycrystalline nature of the nanostructured films deposited by the NPDS under rough vacuum conditions during the kinetic spray process [31]. This demonstrates the fragmentation of the initial micro-sized particles into many domains with a small nanosize, which is accompanied by an increase in the number of defective sites. These defect states act as additional reaction sites for oxygen evolution [23].

3.2. Raman Spectra Analysis

Raman analysis was used to confirm the crystal structure, crystal quality, and presence of both ZnO and WO₃ species in the mixed micron powder and nanostructured thin films. The Raman spectrum of the WO₃ micron powder shown in Figure 3a reveals several distinct peaks at 275, 326, 717, and 809 cm⁻¹ [32]. Raman peaks at 275 and 326 cm⁻¹ correspond to the stretching and bending vibrations of the lattice oxygenated bonds (W–O), respectively [33]. Meanwhile, the observed Raman peaks at higher Raman shift values of 717 and 807 cm⁻¹ increase from several stretching vibrations related to W^{VI+}–O of the monoclinic crystal structure, corresponding to the stretching vibrations of the bridging oxygen [34]. The prominent peaks detected at 807, 717, and 275 cm⁻¹ exhibited distinct intensities and were characteristic vibrational modes of crystalline WO₃ (monoclinic phase) [35–37]. The Raman spectrum of the ZnO powder in Figure 3a shows several distinct peaks at 329, 380, 436, and 1154 cm⁻¹. The A₁-symmetry mode at 380 cm⁻¹ represents the first-order transverse optical (TO) phonon mode [38]. The E_{2L} mode corresponds to the low-frequency vibration of oxygen atoms, whereas the E_{2H} mode corresponds to the high-frequency vibration of heavy zinc (Zn) atoms. [39]. The prominent Raman mode at 329 cm⁻¹ is

primarily associated with the superimposition of second-order optical phonon vibration ($E_{2H}-E_{2L}$) [40,41]. The most prominent Raman peak at 436 cm^{-1} is related to the E_{2H} symmetry and nonpolar second-order vibration of the hexagonal crystalline structure of zinc oxide [42,43]. However, 1154 cm^{-1} represents the second-order vibration mode in ZnO. Similarly, the Raman spectrum for ZnO-WO₃ (10%) mixed micron powder was observed, with all Raman peaks for WO₃ powder (275, 717, and 809 cm^{-1}) corresponding to the (W-O) lattice bond and stretching vibration related to $W^{VI+}-O$ (Figure 3a). In addition, the peak at 326 cm^{-1} of WO₃ vanished in the ZnO-WO₃ (10%) mixed micron powder because of its proximity to the ZnO powder peak at 329 cm^{-1} . However, 380, 436, and 1154 cm^{-1} peaks of ZnO powder corresponding to the first-order TO phonon mode and superimposition of second-order optical phonon vibration ($E_{2H}-E_{2L}$) were present in the Raman spectra of the ZnO-WO₃ (10%) powder (Figure 3a).

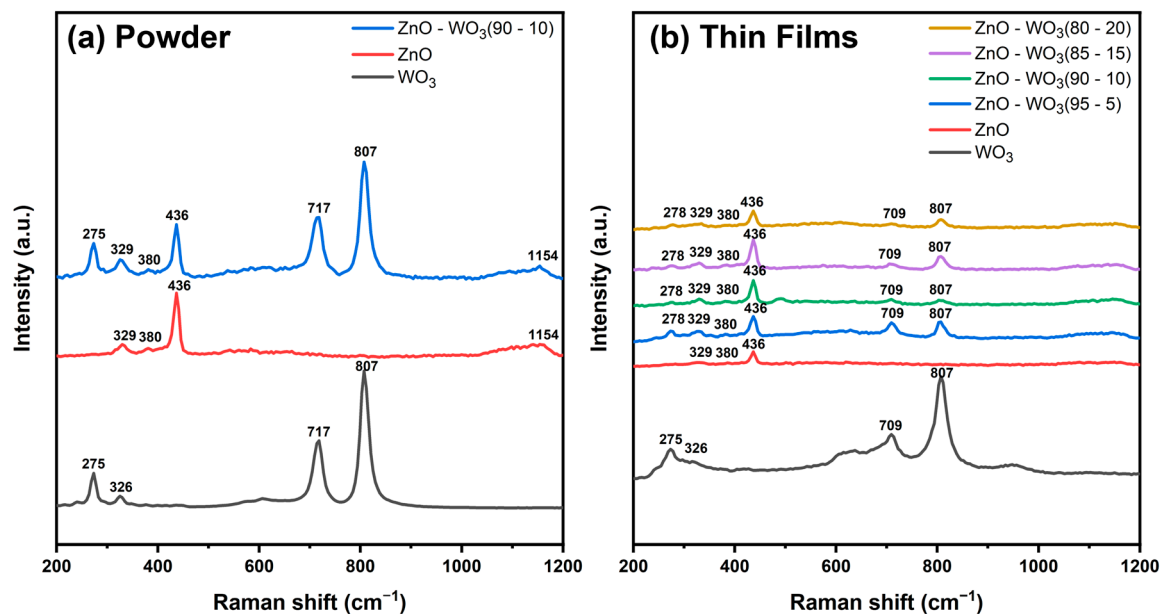


Figure 3. Raman spectra of WO₃, ZnO, and ZnO-WO₃ (10%) powders (a) and WO₃, ZnO, and ZnO-WO₃ (5%, 10%, 15%, and 20%) thin films on fluorine-doped tin oxide (b).

Figure 3b shows the Raman peaks for ZnO on the FTO substrate, indicating all peaks of the powder, which are 329, 380, and 436 cm^{-1} , without any change in peak position, demonstrating that the hexagonal structure remained the same after deposition. The main peak, known as E_2 (high) at 436 cm^{-1} , is the fingerprint of the wurtzite crystal structures [44]. Peaks at 275, 326, and 807 cm^{-1} for WO₃ nanostructure thin films show no change compared with powder peaks; however, the peak at 717 cm^{-1} shifted to 709 cm^{-1} , indicating poor crystalline quality and fragmentation of WO₃ particle size from micro to nano, as explained in the SEM analysis. Furthermore, ZnO-WO₃ thin films on the FTO are shown in Figure 3b. All hybrid thin films showed the same peaks of ZnO and WO₃. The observed peak at 275 cm^{-1} for WO₃ showed a positive shift to 278 cm^{-1} for hybrid thin films, indicating an interaction between ZnO and WO₃. However, the 717 cm^{-1} peak in the WO₃ powder shifted negatively to 709 cm^{-1} , indicating a decrease in the crystalline quality and overall fragmentation by lattice disorder, as explained in the XRD analysis.

3.3. SEM Analysis

The surface morphologies of ZnO, WO₃, and ZnO-WO₃ with 10% WO₃ powder were measured using SEM (Model: S-4800, Hitachi High-Technologies) (Figure S1). The shapes and sizes of the ZnO and WO₃ particles were observed. The size of the WO₃ microparticle powder ranges $<50\text{ }\mu\text{m}$. However, ZnO powder showed multiple variations in sheets and rods with particles ranging $<25\text{ }\mu\text{m}$. Similarly, the presence of both zinc oxide and tungsten

oxide particles was visible in the ball-milled ZnO–WO₃ (10%) mixture before deposition of similar shapes and sizes <25 μm.

Figure 4a shows WO₃ deposited on the FTO substrate; the particle size was significantly reduced from 25 μm to <500 nm, and the SEM image showed several nanosheets. This could be due to the dispersion of the grains in each particle after deposition because of high kinetic energy or the impact between accelerated microparticles and the substrate, causing microparticles to fracture to a smaller nanosize during deposition. When a ZnO thin film was deposited on FTO, multiple variations in nanosheets and nanorods with particle sizes ranging <500 nm were observed (Figure 4b). Therefore, large particles of ZnO and WO₃ were fragmented into smaller particles (particularly of grain size before deposition) because of the accelerated particles with high-impact energy collision with the metallic substrate (FTO) (Figure S1a,b). The SEM morphologies of the hybrid ZnO–WO₃ (5%, 10%, 15%, and 20%) thin films are shown in Figures 4c and 5a–c. All hybrid nanocomposites contain particles of similar shape and size (<500 nm). An overall uniform distribution of particles is observed in the microscale micrographs of all thin films. The shift from microscale powder to nanosized particles in all NC thin films resulted in more defective sites, which acted as more reaction sites, as explained in the XRD analysis.

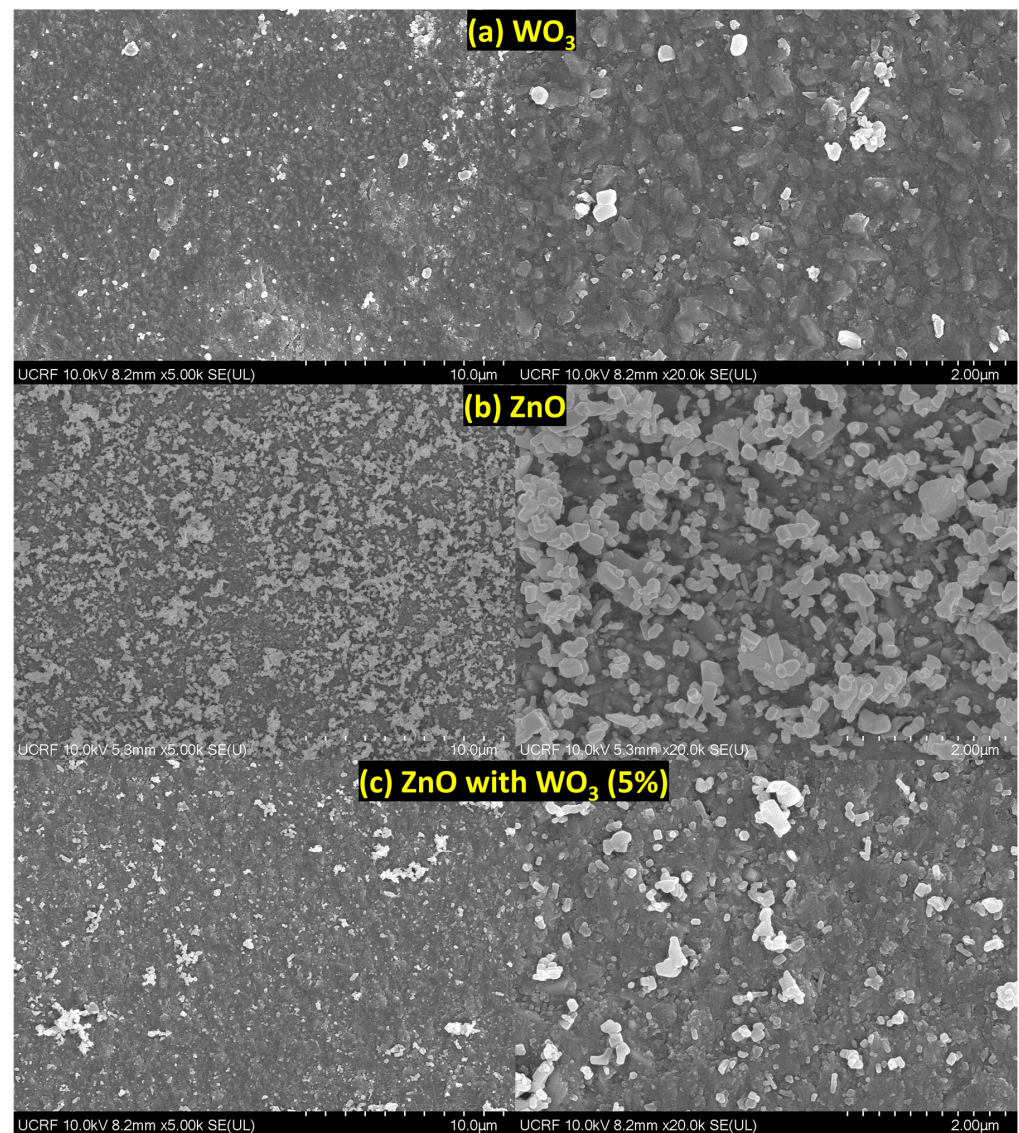


Figure 4. Scanning electron microscopy images of WO₃ (a), ZnO (b), and ZnO with 5% WO₃ (c) content on fluorine-doped tin oxide.

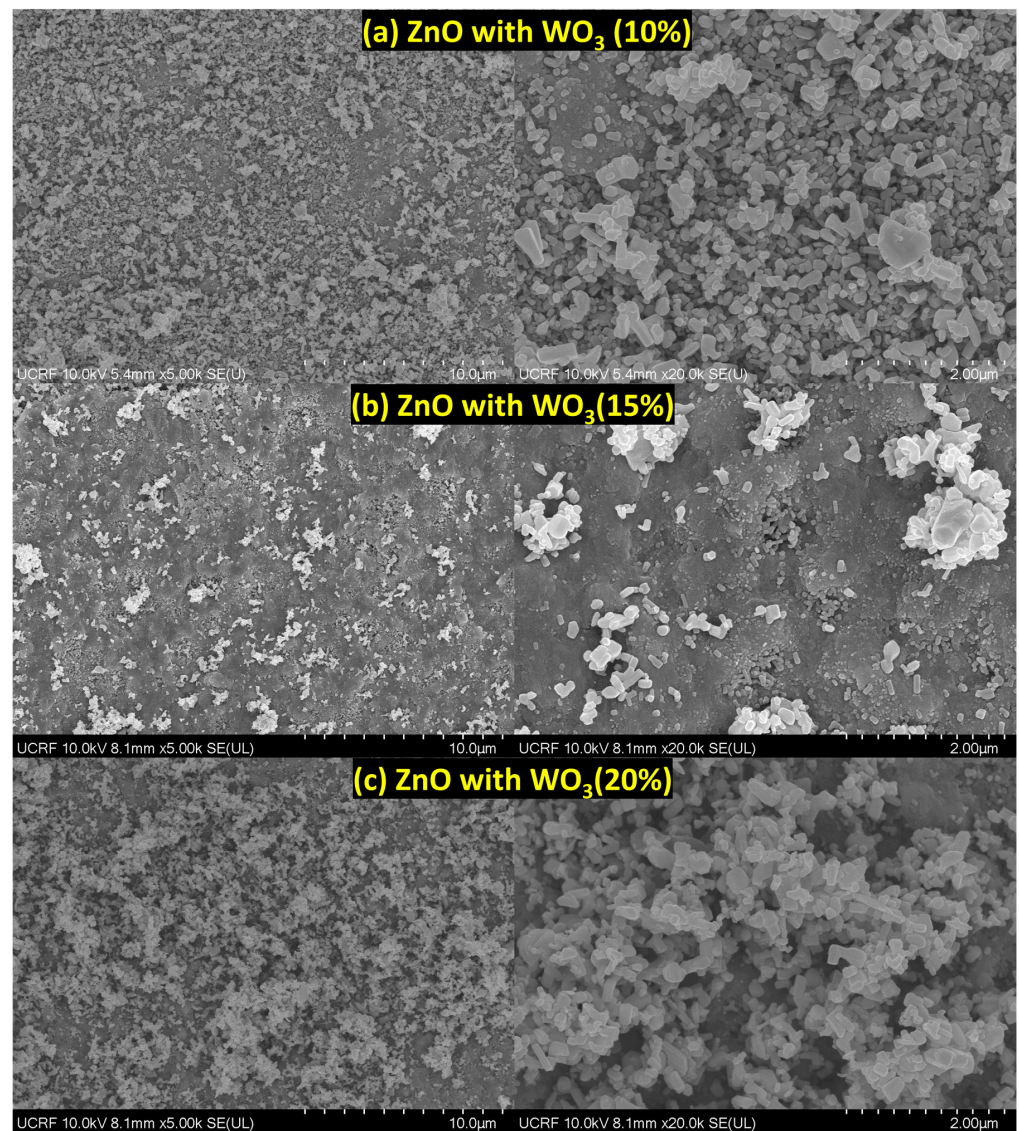


Figure 5. Scanning electron microscopy images of ZnO with 10% (a), ZnO with 15% (b), and ZnO with 20% (c) WO_3 content on fluorine-doped tin oxide.

3.4. XPS Analysis of ZnO– WO_3 NCs

The interfacial chemical bonding states on ZnO NSs, WO_3 NSs, and ZnO– WO_3 hybrid NCs at different WO_3 contents (5, 10, 15, and 20 wt.% WO_3) were investigated using XPS survey spectra (Figure 6a), which revealed the presence of typical signals corresponding to Zn, W, C, Sn, and O elements. These signals were characterized by the active states of ZnO, WO_3 , and FTO from the holding substrate. The high-magnified XPS scans of W 4f, Zn 2p, and O 1s are illustrated in Figure 6b–d.

Figure 7a–e shows the deconvolute XPS scans of the Zn 2p band for both pure ZnO NSs and ZnO– WO_3 hybrid NCs at various WO_3 contents: 5 wt.%, 10 wt.%, 15 wt.%, and 20 wt.%. In the high-resolution Zn 2p XPS scan of pure ZnO NSs, two distinct subband peaks were observed, attributing to Zn $2p_{3/2}$ and Zn $2p_{1/2}$ at 1021.48 and 1044.57 eV, respectively. The estimated peaks in the ZnO– WO_3 NCs at various WO_3 contents are shown in Table 1. The average energy separation between Zn $2p_{3/2}$ and Zn $2p_{1/2}$ was approximately 23.09, which corresponds to the metallic Zn phases [45]. The binding energy of the deconvolute Zn 2p peaks negatively shifts with increasing WO_3 content up to 5 wt.%; however, increasing WO_3 contents (10 wt.%–20 wt.%) causes a positive shift in binding energy to a higher value than with ZnO NCs. This indicated that improving surface bonding and synergy between

ZnO and WO₃ in the hybrid NCs could enhance the interfacial electron density at ZnO grain boundaries (Table 1).

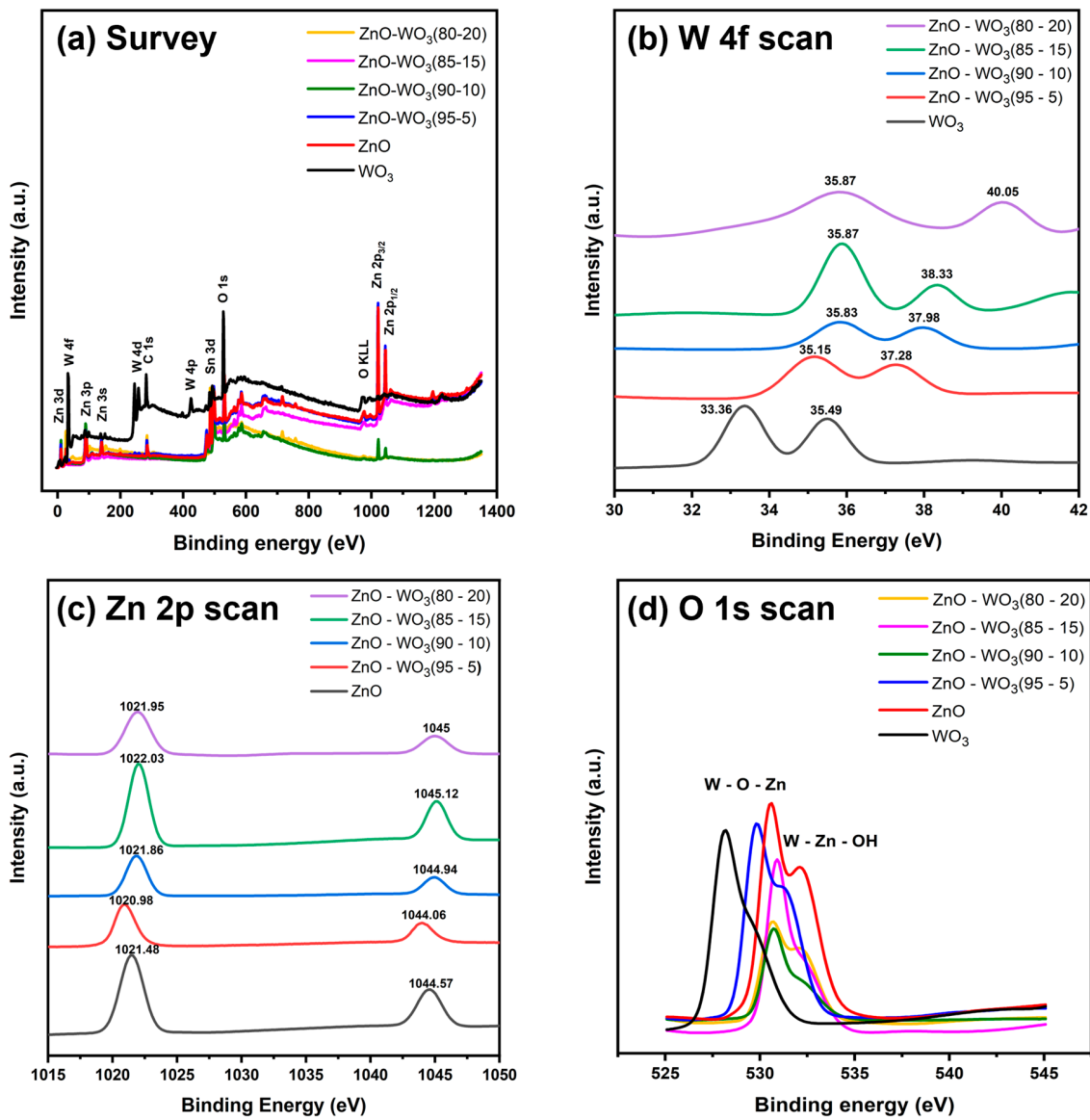


Figure 6. X-ray photoelectron spectroscopy (XPS) survey spectrum (a), high-magnified W 4f (b), Zn 2p (c), and O 1s (d) XPS scans of ZnO–WO₃ hybrid nanocomposites deposited on fluorine-doped tin oxide.

Table 1. Band centers deconvoluted Zn 2p, O 1s, and W 4f X-ray photoelectron spectroscopy scans of ZnO–WO₃ nanocomposite hybrid photoanodes at various WO₃ contents (wt.%).

Band	Binding Energy (eV)					
	WO ₃	ZnO–WO ₃ (80–20%)	ZnO–WO ₃ (85–15%)	ZnO–WO ₃ (90–10%)	ZnO–WO ₃ (95–5%)	ZnO
W 4f	33.36	35.87	35.87	35.83	35.15	-
	35.49	40.05	38.33	37.98	37.28	-
O 1s	528.04	530.56	530.83	530.66	529.72	530.49
	529.24	532.14	531.90	531.90	531.27	532.16
Zn 2p	-	1021.95	1022.03	1021.86	1020.98	1021.48
	-	1045	1045.12	1044.94	1044.06	1044.57

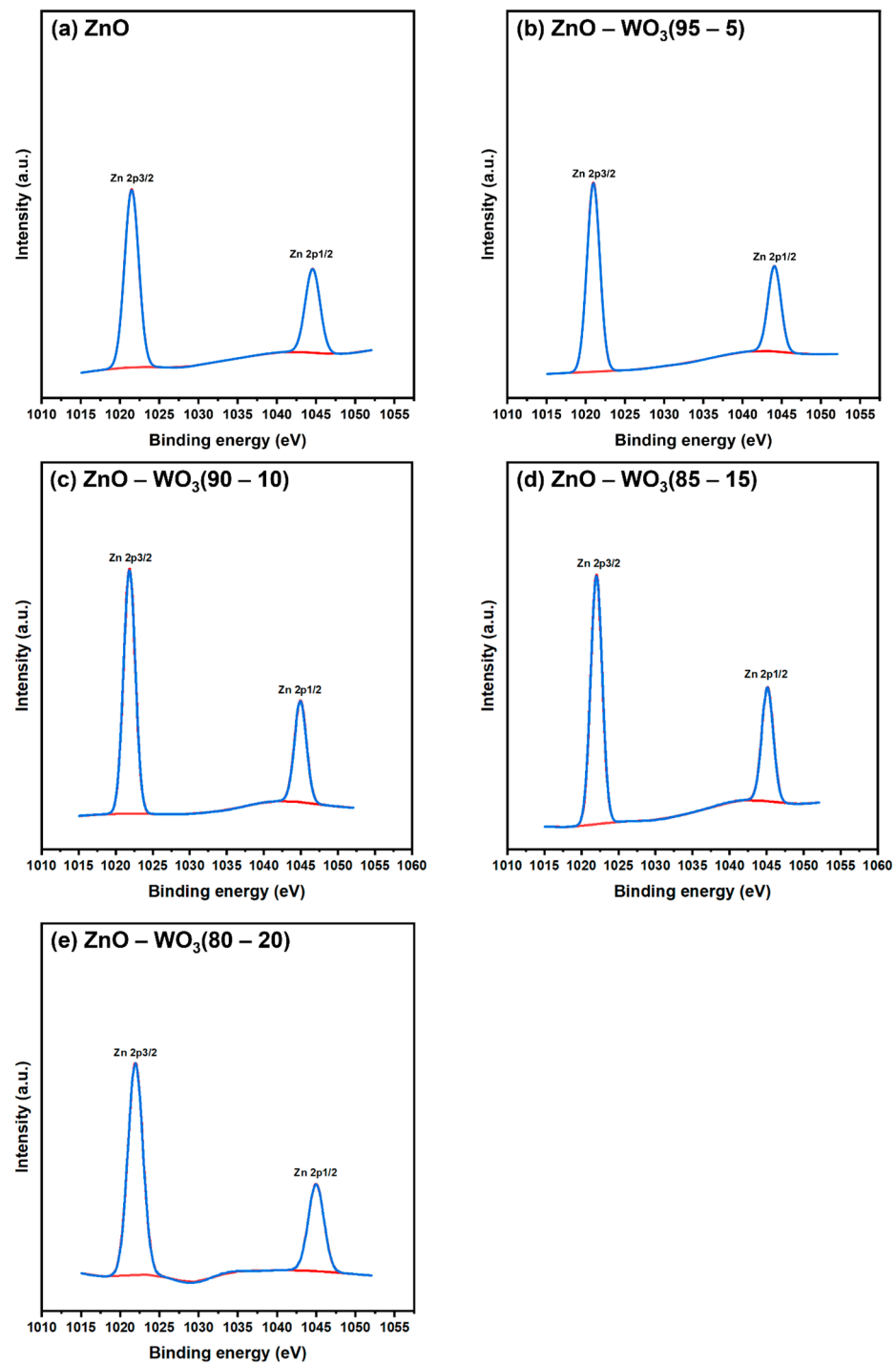


Figure 7. Deconvoluted Zn 2p scans of ZnO NSs (a) and ZnO-WO₃ NCs with 5 wt.% (b), 10 wt.% (c), 15 wt.% (d), and 20 wt.% (e) WO₃.

Figure 8a shows high-resolution deconvoluted O 1s scans of WO₃ NSs with double degenerate binding states at 530.49 and 532.16 eV [46,47]. These bands showed the presence of oxygenated bonds, including internal lattice oxygen (W–O) and adsorbed water molecules (W–OH) [48]. However, the characteristic oxygenated bonds shown in Figure 8b of ZnO were detected at 528.04 and 529.24 eV, which are attributed to Zn–O and Zn–OH, respectively [15,49]. The deconvolute O 1s scans of ZnO-WO₃ NCs at various WO₃ contents (5–20 wt.%) are illustrated in Figure 8c–f, and the estimated peak positions are shown in Table 1.

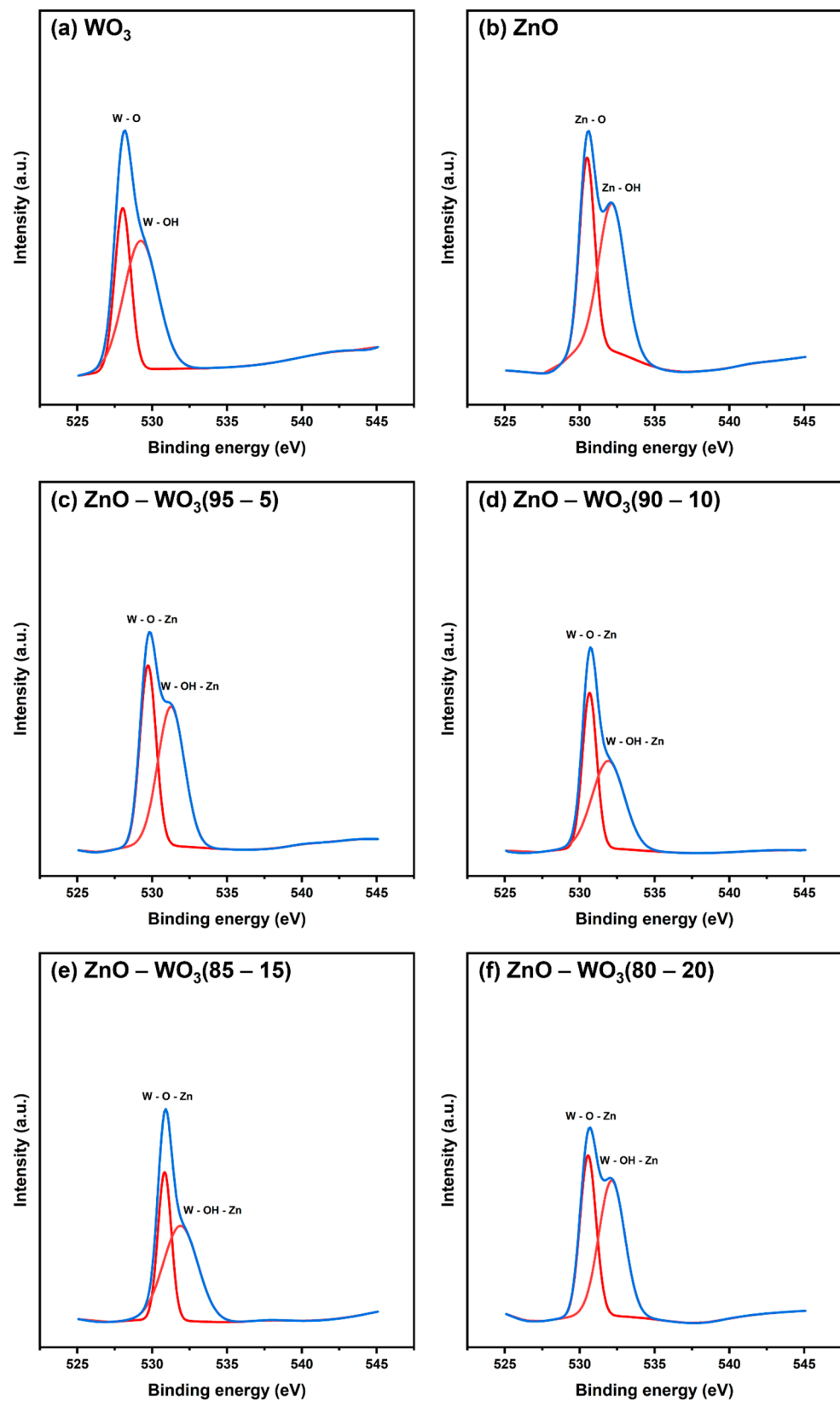


Figure 8. Deconvoluted O 1s X-ray photoelectron spectroscopy scans of WO_3 NSs (a), ZnO NSs (b), and hybrid ZnO- WO_3 NCs at 5 wt.% (c), 10 wt.% (d), 15 wt.% (e), and 20 wt.% (f) WO_3 .

Figure 9a shows deconvoluted W 4f XPS scans of pure WO_3 NSs, which demonstrated the presence of W $4f_{7/2}$ at 33.36 eV and W $4f_{5/2}$ at 35.49 eV and a small peak of $5p_{3/2}$ in

WO_3 [50,51]. Furthermore, ZnO with WO_3 (5%, 10%, 15%, and 20%) heterostructure thin films in all three main peaks are shown in Figure 9b–e, and their values are listed in Table 1. The heterostructure nanocomposites with different WO_3 contents showed that increasing the WO_3 content leads to a positive binding energy peak shift for both $4f_{7/2}$ and $4f_{5/2}$ peaks, demonstrating the strong coupling between WO_3 and ZnO in the deposited heterostructure films within the nanoscale range. Additionally, this obvious positive shift can be due to the presence of interfacial charge transfer from WO_3 to ZnO in the ZnO/ WO_3 heterojunction interface. When WO_3 and ZnO are combined in different compositions, the formation of heterojunctions between the two semiconductors means that the WO_3 semiconductor will transfer interfacial charge to the ZnO semiconductor through the formed interface, thus leading to an increase in W binding energy (Figure 6b) and a decrease in Zn binding energy [52]. More W content means more charge transfers. Furthermore, it is also visible in estimated valence band position that the conduction band position of WO_3 is -3.35 eV above ZnO at -0.65 eV.

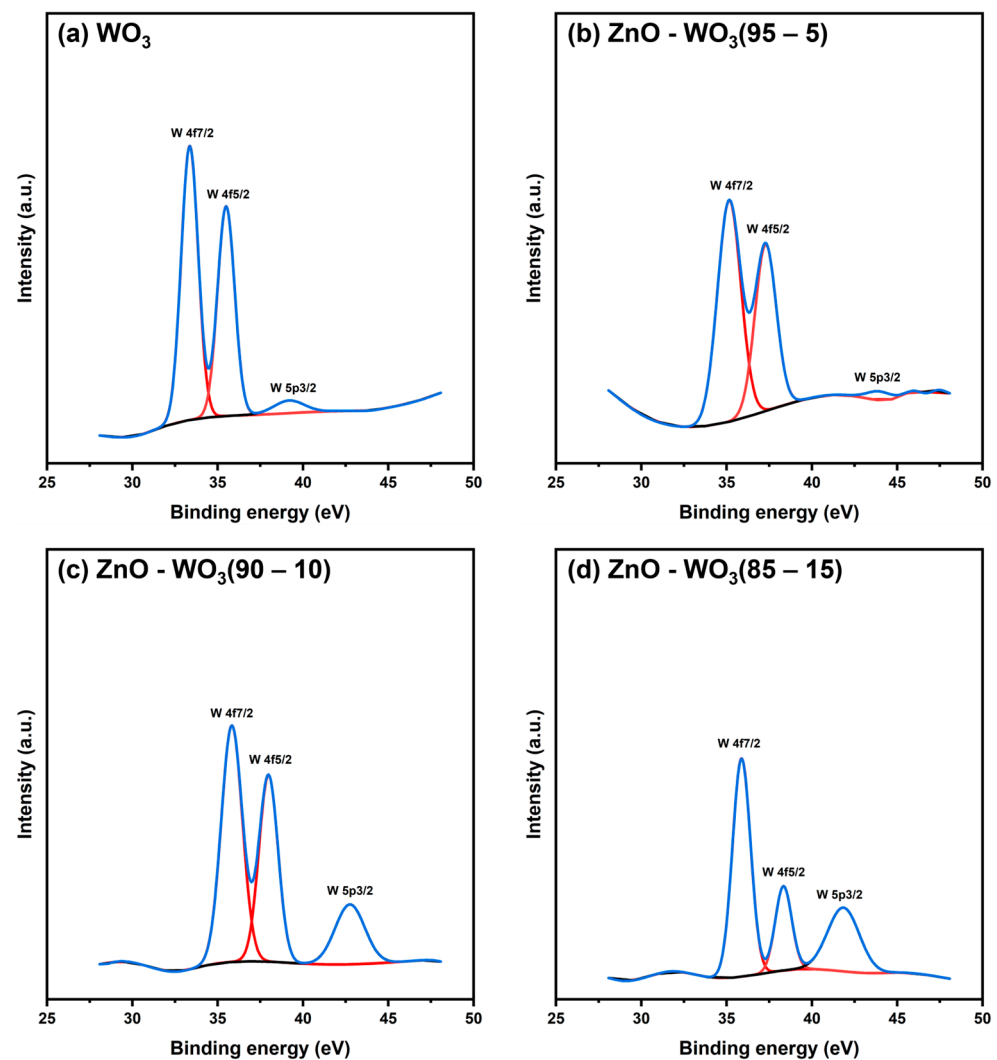


Figure 9. Cont.

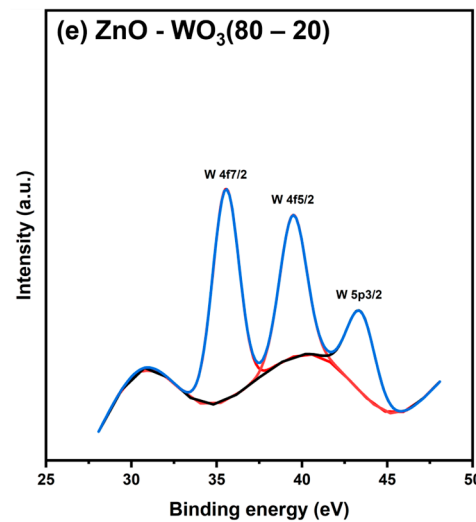


Figure 9. Deconvoluted W 4f X-ray photoelectron spectroscopy scan of WO₃ (a), 5% WO₃ (b), 10% WO₃ (c), 15% WO₃ (d), and 20% WO₃ (e) heterostructure thin films.

3.5. Analysis of the Optical Bandgap of ZnO–WO₃ Hybrid NCs

Diffuse reflectance (R%) spectroscopy was used to examine the optical properties of pure ZnO nanosheets, WO₃ nanosheets, and ZnO–WO₃ NC hybrid photoanodes at different weight ratios of WO₃ (5 wt.%, 10 wt.%, 15 wt.%, and 20 wt.%) in the wavelength range of 200–799 nm (Figure 10a,b). Tauc's plots of ZnO–WO₃ NCs at different WO₃ contents are shown in Figure 10a, where linear extrapolation in the high energy region provided the optical bandgap value of direct bandgap semiconductors according to Equation (2) [53,54].

$$\frac{\alpha}{S} = F = \frac{(1 - R)^2}{2 \times R} \quad (2)$$

$$(\alpha h\nu)^2 = C(h\nu - E_g) \quad (3)$$

where α is the absorption coefficient, ν is the incident light frequency, E_g is the optical bandgap energy, h is the Planck constant, C is the proportionality constant, and S is the scattering coefficient.

The estimated E_g values of pure nanostructured thin films of WO₃ and ZnO are 2.8 and 3.25 eV, respectively. The incorporation of WO₃ into the hybrid NCs did not significantly affect the band structure of the ZnO host lattice, where the estimated E_g values in ZnO–WO₃ hybrid NCs at WO₃ ratios of 5, 10, 15, and 20 wt.% were 3.26, 3.20, 3.264, and 3.27 eV, respectively.

Figure 11a shows the valence band position construction using the XPS survey spectra for binding energies ranging from -3 to 6 eV. The estimated valence band position of ZnO nanosheets is 2.59 eV, that of WO₃ nanosheets is -0.55 eV, and that of ZnO–WO₃ hybrid NCs at different WO₃ contents of 5, 10, 15, and 20 wt.% are 1.95 , 1.77 , 2.44 , and 2.15 eV, respectively (Figure 11b). When energy is absorbed that exceeds the bandgap of the semiconductor, electrons in the valence band (VB) are excited, whereas holes remain in the VB. These holes participate in water oxidation to produce O₂. To facilitate water splitting, the VB potential must exhibit a more positive value than the redox potential of O₂/H₂O, which is equivalent to 1.23 eV. The incorporation of WO₃ in ZnO negatively shifts the valence position in the ZnO–WO₃ hybrid NCs.

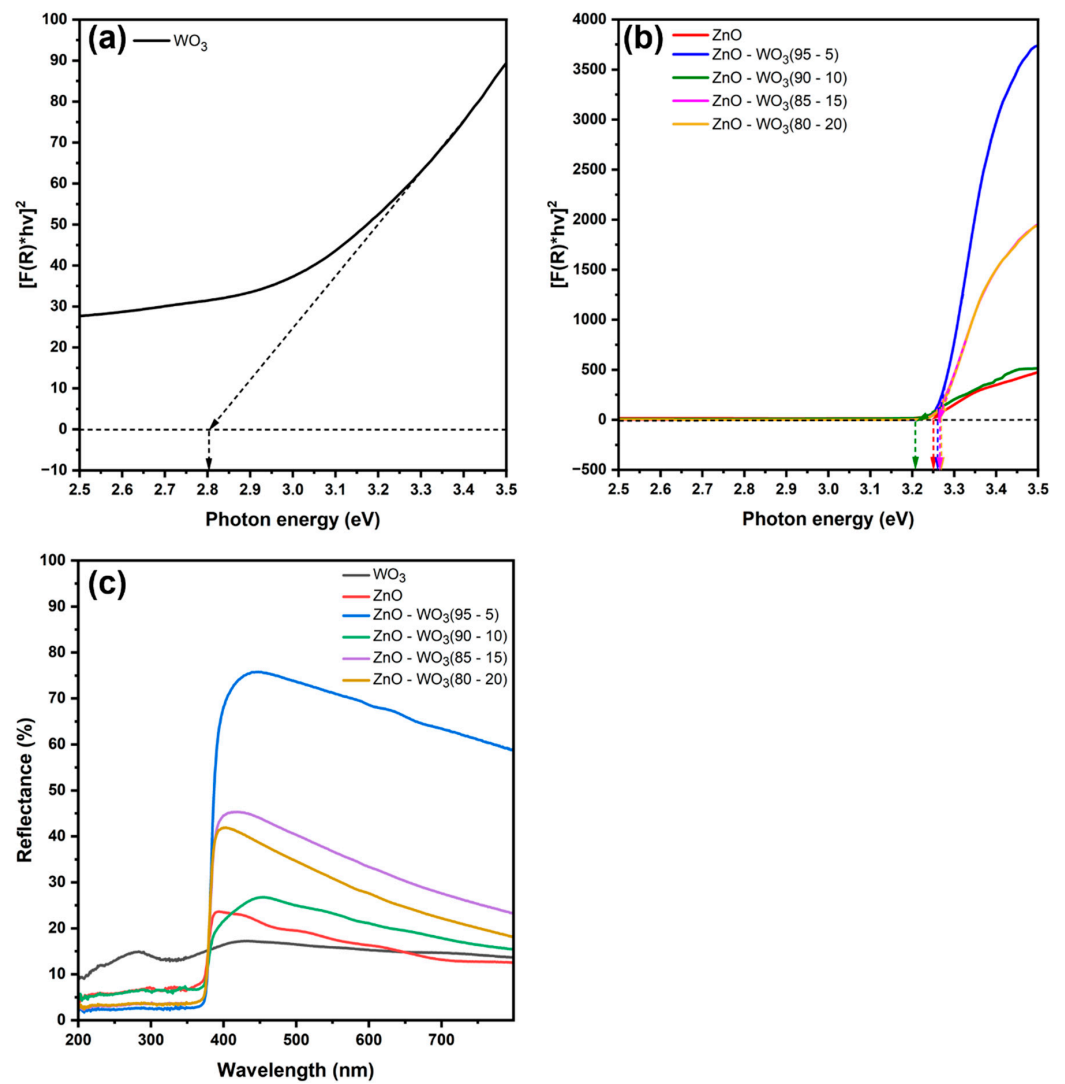


Figure 10. Calculated Tauc's plot of WO₃ (a), the calculated Tauc's plot (b), and ultraviolet–visible diffuse reflectance spectra (c) of ZnO–WO₃ hybrid nanocomposites photoanodes.

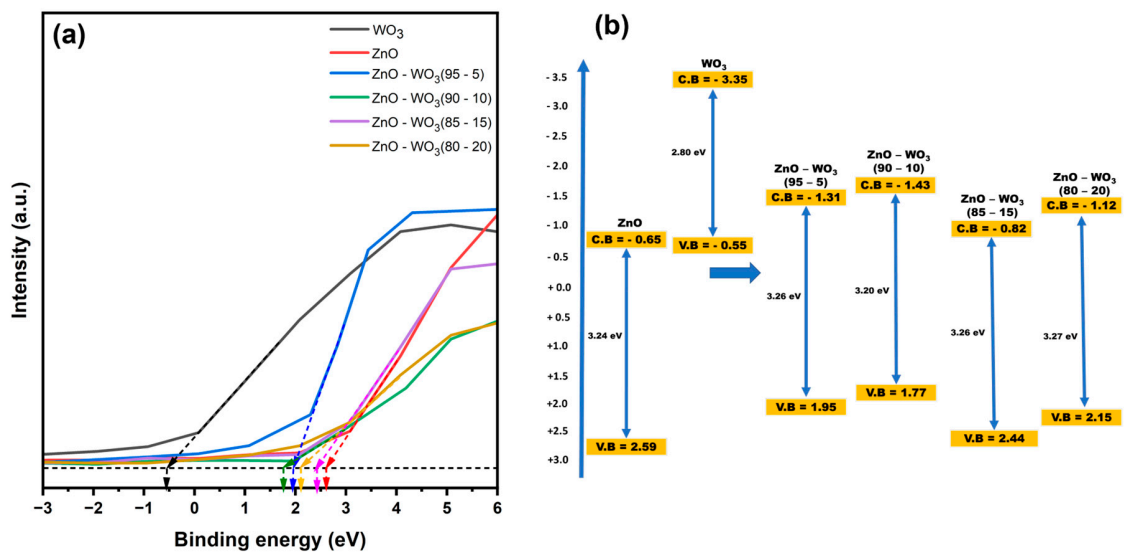


Figure 11. Valence band calculation from the survey spectra of ZnO, WO₃, and ZnO–WO₃ (5%, 10%, 15%, 20%) (a). Bandgap structure of all photoanodes (b).

3.6. Photoluminescence Emission Behavior of ZnO–WO₃ Hybrid NCs

Photoluminescence (PL) emission spectroscopy is more sensitive than normal optical absorbance to localized states induced by interfacial structural defects. The depth of these states within the forbidden gap can be determined by observing defect-related PL spectra arising from the recombination of trapped charge carriers with photogenerated holes [55]. In this study, the effect of interfacial hybridization between WO₃ and ZnO species in ZnO–WO₃ NCs at different WO₃ contents was monitored using PL emission spectra (Figure 12).

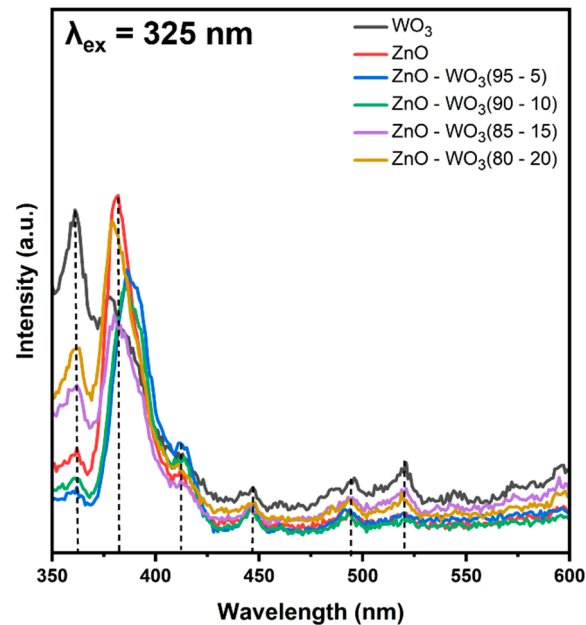


Figure 12. Photoluminescence emission spectra of ZnO NSs, WO₃ NSs, and ZnO–WO₃ hybrid nanocomposites at various WO₃ content.

The PL emission spectrum of ZnO NSs in Figure 12 at an excitation wavelength of 325 nm exhibited broad emission in the UV–visible spectral region [56], with observed emission peaks at 362, 382, 411, 445, 494, and 520 nm. The UV emission bands at 362 and 382 nm were ascribed to fundamental band-edge emission and excitonic recombination [55,57]. The PL emission in the violet–blue spectra region at 411 and 445 nm was attributed to the trapped electrons recombining with photogenerated holes. These trapped electrons are located at shallow trapping levels, where they are linked to either interstitial zinc or oxygen vacancies [58]. The recombination of trapped electrons at deep trapping sites of single oxygen vacancies with photogenerated holes was mainly due to green emission around 520 nm [59–61]. Although the estimated optical bandgap of WO₃ NSs was lower than that of pure ZnO NSs (Figure 10a,b), similar emission behavior was observed. The most intense UV emission band of the WO₃ NSs was observed at a lower wavelength of 362 nm than that of the ZnO NSs (378 nm). However, other emission bands were observed in the visible spectral range, covering violet (411 nm), blue (453 and 487 nm), and green (523 nm) emission bands [62]. The emission bands observed in the blue–green spectral region (453 and 487 nm) lie in the same energy range as the WO₃ bandgap (~2.8 eV). Therefore, they could be attributed to fundamental interband transitions [63–65]. The green emission observed at 523 nm occurred at an energy lower than the bandgap of WO₃, which is ascribed to the recombination of trapped electrons in deep-localized oxygen vacancies with photogenerated holes [66]. Similar emission bands were observed in ZnO–WO₃ hybrid NCs at different WO₃ contents (5 wt.%, 10 wt.%, 15 wt.%, and 20 wt.%). Generally, the hybridization between ZnO and WO₃ led to a decrease in the PL emission intensity compared with the pure phases of ZnO and WO₃, indicating quenching of

the photogenerated carrier recombination rates. This behavior indicates an improvement in synergy in hybrid NCs, which is accompanied by an improvement in photon energy conversion efficiency [15,67,68].

3.7. Photoelectrochemical Water Splitting Measurements

PEC water oxidation measurements were performed in a neutral medium of 0.5 M Na_2SO_4 for a modified FTO working electrode with ZnO nanosheets, WO_3 nanosheets, and a ZnO– WO_3 hybrid (NCs at various WO_3 contents of 5 wt.%, 10 wt.%, 15 wt.%, and 20 wt.%). Figure 13a shows the photocurrent response of all modified photoanodes in the potential range of 0–1.5 V vs. the RHE (i.e., from –0.5 to 1 vs. Hg/HgO). The measured photocurrent ZnO– WO_3 NC hybrid photoanodes with WO_3 weight ratios of 5, 10, 15, and 20 wt.% were 66, 133, 38, and 31 μA , respectively. The obtained photoresponse current of hybrid ZnO– WO_3 NCs was higher than that of pure nanostructured phases of ZnO (18 μA) and WO_3 nanosheets (6 μA), demonstrating the improvement of photocurrent response compared with the pure phases as a result of the improved synergy between ZnO and WO_3 species in the hybrid NCs, which was accompanied by the enhancement of interfacial charge transfer at the electrode/electrolyte interface. The incident photon-to-current efficiency (IPCE) of the fabricated hybrid photoanodes at different polarization potentials was determined using Equation (4) [69]:

$$\text{IPCE}(\%) = J_{ph} \frac{(1.23 - (V - V_{OCP}))}{P_{light}} \times 100\% \quad (4)$$

where P_{light} is the incident power light density, J_{ph} is the photocurrent density, V is the polarization potential, and V_{OCP} is the change in the open-circuit potential (ΔOCP) under light (Figure 13c). Achieving a higher open-circuit potential is crucial in PEC water splitting because it determines the maximum thermodynamic efficiency of the overall water-splitting process. In this study, ZnO– WO_3 NCs with a 10 wt.% WO_3 hybrid photoanode achieved the highest open-circuit potential (OCP). Higher open-circuit potentials are important for optimal PEC cell operation [70,71]. Figure 13b shows the potential-dependent IPCE (%), which is the calculated IPCE (%) value at 1.23 V vs. the RHE (Table 2).

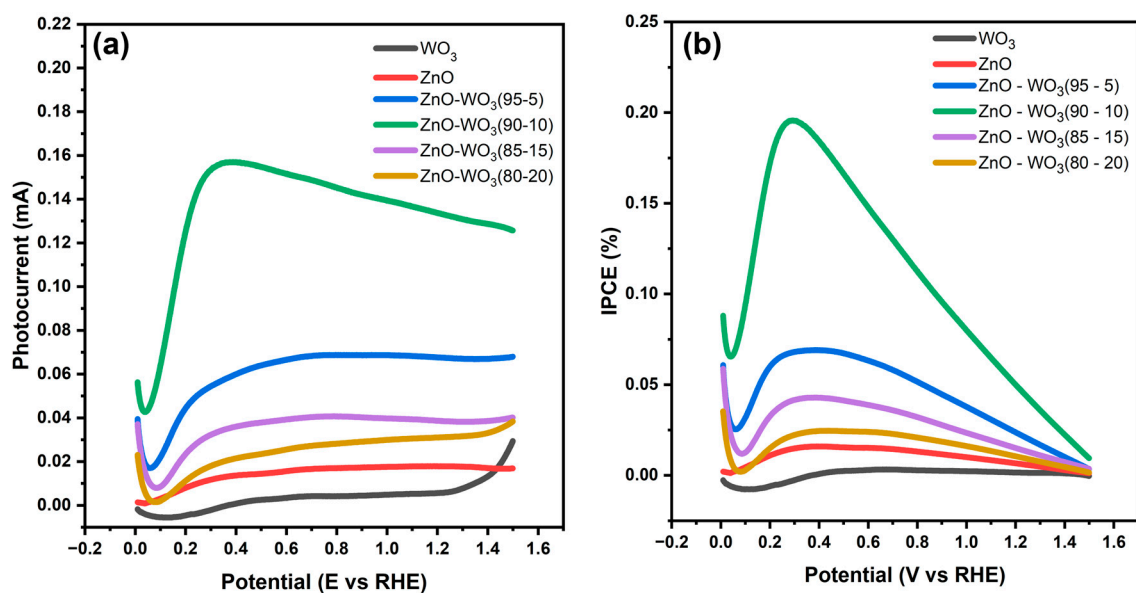


Figure 13. Cont.

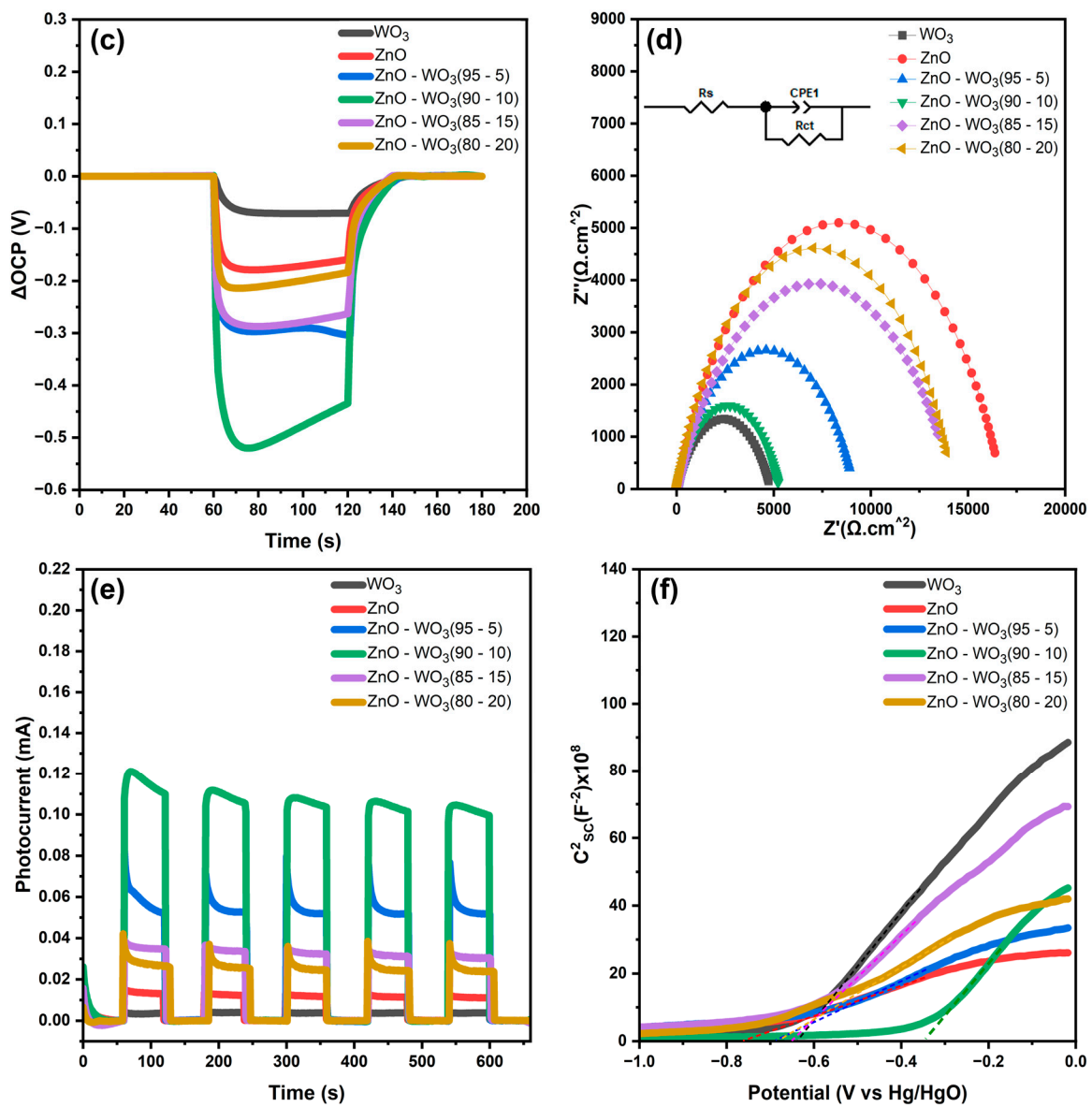


Figure 13. Photoresponse current (a), incident photon conversion efficiency (b), the difference in open-circuit potential (c), Nyquist plots under illumination (d), and chopped chronopotentiometry (e) at 1.23 V vs. the RHE, and M–S plots (f) of ZnO–WO₃ NC photoanodes at various WO₃ %.

Table 2. Photoresponse current (J_{ph}) and photon conversion efficiency (IPCE) of ZnO–WO₃ NC hybrid photoanodes at different WO₃ contents.

Electrodes	Photocurrent (mA·cm ⁻²)	IPCE (%)
WO ₃	0.006	0.003
ZnO	0.018	0.016
ZnO–WO ₃ NCs (5 wt.% WO ₃)	0.066	0.069
ZnO–WO ₃ NCs (10 wt.% WO ₃)	0.133	0.196
ZnO–WO ₃ NCs (15 wt.% WO ₃)	0.038	0.043
ZnO–WO ₃ NCs (20 wt.% WO ₃)	0.031	0.025

Figure 13d shows Nyquist plots of ZnO NSs, WO₃ NSs, and ZnO–WO₃ NC hybrid photoanodes under sunlight illumination at 1.23 V vs. the RHE. The incorporation of WO₃ resulted in a reduction in the charge transfer resistance (R_{ct}) of ZnO–WO₃ hybrid

NCs compared with that of pure ZnO NSs, indicating an enhancement in the kinetics of interfacial charge transfer. To further assess the photoelectrochemical (PEC) capabilities, the Electrical Equivalent Circuit (EEC) model was analyzed for the fabricated photoanodes while being illuminated at 1.23 V_{RHE} (Figure 13d). The accompanying inset illustrates an RC circuit fitted to the data, with R_s representing solution resistance, R_{ct} denoting interfacial charge transfer resistance between the photoanode and electrolyte interfaces, and CPE as a constant phase element. Table 3 provides the calculated values of R_{ct}, R_s, and CPE based on the equivalent circuit scheme. The consistent R_s values of 10 Ω (± 4 Ω) across all samples reflect stable solution conditions. However, the observed R_{ct} value of ZnO–WO₃ (90–10) (5270 Ω) is markedly lower compared to ZnO and other nanocomposites. This lower R_{ct} for the ZnO–WO₃ (90–10) interface indicates efficient separation of photogenerated electrons and holes in the photoanodes, attributed to the effective consumption of holes in the electrolyte solution. Furthermore, the semicircle diameter in the Nyquist plots represents the charge transfer behavior at the interfaces between the photoanodes and electrolytes. A smaller diameter signifies lower charge transfer resistance, indicating enhanced efficiency in the separation of photogenerated charge carriers [22,72]. Similarly, the stability of the photoresponse current was validated for five complete cycles under dark and illumination states for all, as shown, and hybrid photoanodes in Figure 13e.

Table 3. Equivalent-circuit fitting parameters including nussiance resistance (R_s), charge transfer resistance (R_{ct}), and constant phase element (CPE) capacitance of ZnO–WO₃ NC hybrid photoanodes at different WO₃ contents.

Electrodes	R _s (Ω)	R _{ct} (kΩ)	CPE (F)
WO ₃	8.34	4.82	0.00021
ZnO	10.97	16.76	0.000099
ZnO–WO ₃ NCs (5 wt.% WO ₃) NCs	9.76	9.13	0.00017
ZnO–WO ₃ NCs (10 wt.% WO ₃) NCs	11.43	5.27	0.00016
ZnO–WO ₃ NCs (15 wt.% WO ₃) NCs	8.88	14.22	0.00017823
ZnO–WO ₃ NCs (20 wt.% WO ₃) NCs	13.09	14.56	0.00016

Figure 13f shows Mott–Schottky plots of ZnO NSs, WO₃ NSs, and ZnO–WO₃ NCs at various WO₃ contents (5%, 10%, 15%, and 20%), where the flat band potential (V_{fb}) and the corresponding donor density concentration (N_D) were estimated and recorded in Table 4.

$$\frac{1}{C_{sc}^2} = \frac{1}{2\epsilon\epsilon_0 e A^2 N_D} \left(V - V_{fb} - \frac{k_B T}{e} \right) \quad (5)$$

where *A* is the electrode area, *V* is the applied potential, *e* is the electric charge of an electron, *T* is the absolute temperature, *k_B* is the Boltzmann constant, *ε* is the dielectric constant of ZnO (8.6) [15] and WO₃ (50) [73–75], and *ε₀* is the vacuum electric permittivity.

Table 4. Calculated donor concentration (N_D), flat band potential (V_{fb}), and width of the space charge layer (W_{scl}) of hybrid ZnO–WO₃ nanocomposite photoanodes across varying WO₃ content levels.

Electrode	V _{fb}	N _D × 10 ²⁶	W _{scl} (nm)
WO ₃	−0.64	0.46	12.84
ZnO	−0.78	9.24	1.24
ZnO–WO ₃ NCs (5 wt.% WO ₃)	−0.69	6.70	1.42
ZnO–WO ₃ NCs (10 wt.% WO ₃)	−0.36	2.69	1.96
ZnO–WO ₃ NCs (15 wt.% WO ₃)	−0.65	4.06	1.79
ZnO–WO ₃ NCs (20 wt.% WO ₃)	−0.69	5.70	1.53

The combination of WO₃ with ZnO nanosheets increased the positive shift of V_{fb} for all hybrid photoanodes compared with photoanodes composed solely of pure ZnO NSs. Compared to all hybrid photoanodes, the hybrid ZnO–WO₃ NCs containing 10 wt.% WO₃

exhibited the highest positive shift. The observed positive shift in V_{fb} indicates improved energy conversion efficiency [76]. However, the concentration of majority carriers (N_D) in n-type semiconductors by a direct route does not correlate with PEC cell performance. This is because N_D represents the concentration of charge carriers that do not participate in the PEC water-splitting reaction that occurs at the interface between the electrode and electrolyte. Despite this, alterations in N_D exert a substantial influence on the positioning of the Fermi level (E_f) concerning the intrinsic energy level (E_i). This relationship is particularly relevant because (E_i) is situated at the center of the modified band structure of the electrode according to the following relationship:

$$E_f = E_i + kT \times \ln\left(\frac{N_D}{n_i}\right) \quad (6)$$

Furthermore, the concentration of minority carriers (holes) within the space charge layer contributes to water oxidation and O_2 evolution during PEC water splitting. The space charge layer formed between the electrode and electrolyte plays a significant role in the performance of energy conversion. According to K. Schwarzburg [77], the separation of photogenerated electron-hole pairs occurs rapidly within picoseconds in the depletion region because of an externally applied potential. In this process, electrons generated by light absorption relocate to the interior bulk area of the photoanode surface, while holes created in the process traverse toward the position between the electrode and electrolyte, contributing to the PEC water splitting process [78]. W_{scl} can be calculated using Equation (7):

$$W_{scl} = \sqrt{\frac{2\epsilon\epsilon_0(V - V_{fb})}{eN_D}} \quad (7)$$

The calculated values for W_{scl} are shown in Table 4. Based on the calculated W_{scl} values, the photoanode ZnO–WO₃ (90–10) showed the highest value compared with the other hybrid photoanodes and pure ZnO/FTO. This explains why the incorporation of WO₃ content in ZnO at a certain limit (10%) enhances the charge kinetics of ZnO–WO₃ hybrid photoanodes and the concentration of photogenerated carriers within the space charge layer located at the interface between the electrode and electrolyte.

4. Conclusions

ZnO–WO₃ NC hybrid photoanodes were deposited on an FTO substrate using a one-step dry NPDS with no additional post-process. The fabricated heterostructure electrodes were used to examine the PEC water splitting in a neutral electrolyte (0.5 M Na₂SO₄); SEM images clearly showed the microparticle transformation of nanosized structures in the deposited thin films. Raman spectra revealed a decrease in crystallinity due to kinetic-induced fragmentation in all hybrid photoanodes at WO₃ contents ranging from 5 to 20 wt.%. High-resolution XPS of the W 4f, Zn 2p, and O 1s bands revealed a negative shift with increasing ZnO content in the hybrid NCs, demonstrating improved interfacial synergy. Analysis of the diffuse reflectance spectra demonstrated that increasing the WO₃ to 10 wt.% reduced the ZnO bandgap from 3.24 to 3.20 eV in the hybrid photoanode. The PL emission spectra revealed that the ZnO with 10 wt.% WO₃ hybrid photoanodes showed the lowest emission intensity, indicating that the dissociation of photogenerated charges was improved. Analysis of Mott–Schottky plots across all hybrid photoanodes indicated a positive shift in the V_{fb} , reduction in N_D , and expansion of the space charge layer width compared with ZnO/FTO. This phenomenon exerted a substantial impact on the effective segregation of photogenerated electron-hole pairs within the space charge layer located at the interface between the electrode and electrolyte, leading to an overall enhancement in PEC water splitting. Note that the introduction of WO₃ into all hybrid heterostructure electrodes increased the photoresponse current and reduced the charge transfer resistance compared with nanoscale ZnO/FTO photoanodes. The ZnO–WO₃ NCs/FTO hybrid

photoanodes with 5%, 10%, 15%, and 20% WO₃ content exhibited photocurrents of 0.066, 0.133, 0.038, and 0.031 mA·cm⁻², respectively, compared with only 0.018 mA·cm⁻² for pure ZnO/FTO and 0.006 mA·cm⁻² for WO₃/FTO photoanodes at 1.23 V vs. the RHE. Furthermore, the maximum IPCE for ZnO–WO₃ hybrid photoanodes exhibited a transition to a lower potential than that for ZnO/FTO and WO₃/FTO photoanodes. The ZnO–WO₃ hybrid photoanode with 10% WO₃ content revealed a maximum efficiency of 0.196%. The stability of the photocurrent for all NS photoanodes was validated for five cycles. The stability test revealed almost the same photocurrents. In contrast to alternative methods for fabricating hybrid ZnO–WO₃ nanocomposite photoanodes, the NC photoanodes in this study were fabricated in a very short time (Table S1) using only the one-step dry NPDS method with commercially available microsized powders mixed with conventional ball milling. In addition, no additional post-processes for binding, cleaning, or drying were required. Finally, a 10% ZnO–WO₃ photoanode outperformed pure ZnO/FTO, WO₃/FTO, and other NC photoanodes in terms of PEC water splitting in a neutral electrolyte.

Supplementary Materials: The following supporting information can be downloaded at: <https://www.mdpi.com/article/10.3390/mi14122189/s1>, Figure S1: Scanning electron microscopy images of ZnO powder (a), WO₃ powder (b), and ZnO–WO₃ composite powder with 10% WO₃ content (c). Table S1. The average consumable time for different material coatings in different techniques. Refs. [79–81] are cited in the Supplementary Materials.

Author Contributions: M.S.M.—Experimentation, Methodology, Validation, Investigation, Writing—original draft. D.R.—Experimentation, Methodology, Investigation, Writing—review and editing. D.-M.C.—Conceptualization, Supervision, Methodology, Resources, Writing—review and editing. A.G.A.-E.—Conceptualization, Methodology, Validation, Investigation, Writing—review and editing. All authors have read and agreed to the published version of the manuscript.

Funding: This research was supported by a National Research Foundation of Korea grant (NRF-2021R1A2C1008248) and by the “Regional Innovation Strategy (RIS)” through the National Research Foundation of Korea (NRF) funded by the Ministry of Education (MOE) (2021RIS-003).

Data Availability Statement: Data are contained within the article and Supplementary Materials.

Conflicts of Interest: The authors declare no conflict of interest.

References

1. Bard, A.J.; Fox, M.A. Artificial Photosynthesis: Solar Splitting of Water to Hydrogen and Oxygen. *Accounts Chem. Res.* **1995**, *28*, 141–145. [CrossRef]
2. Yuan, K.; Cao, Q.; Li, X.; Chen, H.-Y.; Deng, Y.; Wang, Y.-Y.; Luo, W.; Lu, H.-L.; Zhang, D.W. Synthesis of WO₃@ZnWO₄@ZnO-ZnO hierarchical nanocactus arrays for efficient photoelectrochemical water splitting. *Nano Energy* **2017**, *41*, 543–551. [CrossRef]
3. Nguyen, T.; Thuy, T.; Cho, S.K.; Amangeldinova, Y. WO₃–ZnO and CuO–ZnO nanocomposites as highly efficient photoanodes under visible light. *Nanotechnology* **2020**, *31*, 255702.
4. Kalanur, S.S.; Duy, L.T.; Seo, H. Recent Progress in Photoelectrochemical Water Splitting Activity of WO₃ Photoanodes. *Top. Catal.* **2018**, *61*, 1043–1076. [CrossRef]
5. Palmstrom, A.F.; Santra, P.K.; Bent, S.F. Atomic layer deposition in nanostructured photovoltaics: Tuning optical, electronic and surface properties. *Nanoscale* **2015**, *7*, 12266–12283. [CrossRef] [PubMed]
6. Barreca, D.; Carraro, G.; Gasparotto, A.; Maccato, C.; Altantzis, T.; Sada, C.; Kaunisto, K.; Ruoko, T.; Bals, S. Vapor Phase Fabrication of Nanoheterostructures Based on ZnO for Photoelectrochemical Water Splitting. *Adv. Mater. Interfaces* **2017**, *4*, 1700161. [CrossRef]
7. Chen, Y.; Wang, L.; Gao, R.; Zhang, Y.-C.; Pan, L.; Huang, C.; Liu, K.; Chang, X.-Y.; Zhang, X.; Zou, J.-J. Polarization-Enhanced direct Z-scheme ZnO-WO_{3-x} nanorod arrays for efficient piezoelectric-photoelectrochemical Water splitting. *Appl. Catal. B Environ.* **2019**, *259*, 118079. [CrossRef]
8. Wang, G.; Wang, H.; Ling, Y.; Tang, Y.; Yang, X.; Fitzmorris, R.C.; Wang, C.; Zhang, J.Z.; Li, Y. Hydrogen-treated TiO₂ nanowire arrays for photoelectrochemical water splitting. *Nano Lett.* **2011**, *11*, 3026–3033. [CrossRef]
9. Mishra, M.; Chun, D.-M. α-Fe₂O₃ as a photocatalytic material: A review. *Appl. Catal. A Gen.* **2015**, *498*, 126–141. [CrossRef]
10. Sivula, K.; Le Formal, F.; Grätzel, M. Solar water splitting: Progress using hematite (α-Fe₂O₃) photoelectrodes. *ChemSusChem* **2011**, *4*, 432–449. [CrossRef]
11. Su, J.; Guo, L.; Bao, N.; Grimes, C.A. Nanostructured WO₃/BiVO₄ heterojunction films for efficient photoelectrochemical water splitting. *Nano Lett.* **2011**, *11*, 1928–1933. [CrossRef] [PubMed]

12. Zhu, T.; Chong, M.N.; Chan, E.S. Nanostructured tungsten trioxide thin films synthesized for photoelectrocatalytic water oxidation: A review. *ChemSusChem* **2014**, *7*, 2974–2997. [[CrossRef](#)] [[PubMed](#)]
13. Palmas, S.; Castresana, P.A.; Mais, L.; Vacca, A.; Mascia, M.; Ricci, P.C. TiO₂–WO₃ nanostructured systems for photoelectrochemical applications. *RSC Adv.* **2016**, *6*, 101671–101682. [[CrossRef](#)]
14. Wudil, Y.; Ahmad, U.; Gondal, M.; Al-Osta, M.A.; Almohammed, A.; Sa'Id, R.; Hrahsheh, F.; Haruna, K.; Mohamed, M. Tuning of graphitic carbon nitride (g-C₃N₄) for photocatalysis: A critical review. *Arab. J. Chem.* **2023**, *16*. [[CrossRef](#)]
15. Abd-Elrahim, A.; Chun, D.-M. Facile one-step deposition of ZnO-graphene nanosheets hybrid photoanodes for enhanced photoelectrochemical water splitting. *J. Alloys Compd.* **2021**, *870*, 159430. [[CrossRef](#)]
16. Rao, P.M.; Cai, L.; Liu, C.; Cho, I.S.; Lee, C.H.; Weisse, J.M.; Yang, P.; Zheng, X. Simultaneously efficient light absorption and charge separation in WO₃/BiVO₄ Core/shell nanowire photoanode for photoelectrochemical water oxidation. *Nano Lett.* **2014**, *14*, 1099–1105. [[CrossRef](#)]
17. Kim, M.-S.; Chun, D.-M.; Choi, J.-O.; Lee, J.-C.; Kim, K.-S.; Kim, Y.H.; Lee, C.S.; Ahn, S.-H. Room temperature deposition of TiO₂ using nano particle deposition system (NPDS): Application to dye-sensitized solar cell (DSSC). *Int. J. Precis. Eng. Manuf.* **2011**, *12*, 749–752. [[CrossRef](#)]
18. Galán-González, A.; Sivan, A.K.; Hernández-Ferrer, J.; Bowen, L.; Di Mario, L.; Martelli, F.; Benito, A.M.; Maser, W.K.; Chaudhry, M.U.; Gallant, A.; et al. Cobalt-Doped ZnO Nanorods Coated with Nanoscale Metal–Organic Framework Shells for Water-Splitting Photoanodes. *ACS Appl. Nano Mater.* **2020**, *3*, 7781–7788. [[CrossRef](#)]
19. Han, J.; Liu, Z. Optimization and Modulation Strategies of Zinc Oxide-based Photoanodes for Highly Efficient Photoelectrochemical Water Splitting. *ACS Appl. Energy Mater.* **2021**, *4*, 1004–1013. [[CrossRef](#)]
20. Zhang, J.; Zhu, G.; Liu, W.; Xi, Y.; Golosov, D.; Zavadski, S.; Melnikov, S. 3D core-shell WO₃@α-Fe₂O₃ photoanode modified by ultrathin FeOOH layer for enhanced photoelectrochemical performances. *J. Alloys Compd.* **2020**, *834*, 154992. [[CrossRef](#)]
21. Xu, Y.; Cao, Q.; Yi, Z.; Wu, P.; Cai, S. Adjusting the energy bands of WO₃@ZnO nanocomposite heterojunction through the combination of WO₃ thin film to improve its photoelectric performance. *IEEE Access* **2020**, *8*, 171350–171358. [[CrossRef](#)]
22. Ji, J.; Sang, P.; Kim, J.H. Improving the photoelectrochemical performance of spin-coated WO₃/BiVO₄/ZnO photoanodes by maximizing charge transfer using an optimized ZnO decoration layer. *Ceram. Int.* **2021**, *47*, 26260–26270. [[CrossRef](#)]
23. Chun, D.M.; Kim, M.H.; Lee, J.C.; Ahn, S.H. A nano-particle deposition system for ceramic and metal coating at room temperature and low vacuum conditions. *Int. J. Precis. Eng. Manuf.* **2008**, *9*, 51–53.
24. Chun, D.-M.; Ahn, S.-H. Deposition mechanism of dry sprayed ceramic particles at room temperature using a nano-particle deposition system. *Acta Mater.* **2011**, *59*, 2693–2703. [[CrossRef](#)]
25. Chun, D.-M.; Choi, J.-O.; Lee, C.S.; Ahn, S.-H. Effect of stand-off distance for cold gas spraying of fine ceramic particles (<5 μm) under low vacuum and room temperature using nano-particle deposition system (NPDS). *Surf. Coatings Technol.* **2012**, *206*, 2125–2132. [[CrossRef](#)]
26. Abd-Elrahim, A.; Chun, D.-M. Fabrication of efficient nanostructured Co₃O₄–Graphene bifunctional catalysts: Oxygen evolution, hydrogen evolution, and H₂O₂ sensing. *Ceram. Int.* **2020**, *46*, 23479–23498. [[CrossRef](#)]
27. Yogamalar, R.; Srinivasan, R.; Vinu, A.; Ariga, K.; Bose, A.C. X-ray peak broadening analysis in ZnO nanoparticles. *Solid State Commun.* **2009**, *149*, 1919–1923. [[CrossRef](#)]
28. Kalanur, S.S.; Hwang, Y.J.; Chae, S.Y.; Joo, O.S. Facile growth of aligned WO₃ nanorods on FTO substrate for enhanced photoanodic water oxidation activity. *J. Mater. Chem. A* **2013**, *1*, 3479–3488. [[CrossRef](#)]
29. Abd-Elrahim, A.; Chun, D.-M. Nanosized Co₃O₄–MoS₂ heterostructure electrodes for improving the oxygen evolution reaction in an alkaline medium. *J. Alloys Compd.* **2020**, *853*, 156946. [[CrossRef](#)]
30. Kim, H.; Choi, D.; Kim, K.; Chu, W.; Chun, D.-M.; Lee, C.S. Effect of particle size and amorphous phase on the electrochromic properties of kinetically deposited WO₃ films. *Sol. Energy Mater. Sol. Cells* **2018**, *177*, 44–50. [[CrossRef](#)]
31. Mohammed, M.M.; Abd-Elrahim, A.; Chun, D.-M. One-step deposition of a Ni(OH)₂-graphene hybrid prepared by vacuum kinetic spray for high energy density hybrid supercapacitor. *Mater. Chem. Phys.* **2020**, *244*, 122701. [[CrossRef](#)]
32. Daniel, M.; Desbat, B.; Lassegues, J.; Gerand, B.; Figlarz, M. Infrared and Raman study of WO₃ tungsten trioxides and WO₃·xH₂O tungsten trioxide hydrates. *J. Solid State Chem.* **1987**, *67*, 235–247. [[CrossRef](#)]
33. Zheng, J.Y.; Song, G.; Hong, J.; Van, T.K.; Pawar, A.U.; Kim, D.Y.; Kim, C.W.; Haider, Z.; Kang, Y.S. Facile fabrication of WO₃ nanoplates thin films with dominant crystal facet of (002) for water splitting. *Cryst. Growth Des.* **2014**, *14*, 6057–6066. [[CrossRef](#)]
34. Ou, J.Z.; Yaacob, M.H.; Breedon, M.; Zheng, H.D.; Campbell, J.L.; Latham, K.; Plessis, J.D.; Wlodarski, W.; Kalantar-Zadeh, K. In situ Raman spectroscopy of H₂ interaction with WO₃ films. *Phys. Chem. Chem. Phys.* **2011**, *13*, 7330–7339. [[CrossRef](#)] [[PubMed](#)]
35. Wolcott, A.; Kuykendall, T.R.; Chen, W.; Chen, S.; Zhang, J.Z. Synthesis and characterization of ultrathin WO₃ nanodisks utilizing long-chain Poly(ethylene glycol). *J. Phys. Chem. B* **2006**, *110*, 25288–25296. [[CrossRef](#)] [[PubMed](#)]
36. Spectroscopies, Y.; Shigesato, Y.; Murayama, A.; Kamimori, T.; Matsuhira, K. Characterization of Evaporated Amorphous WO₃ Films. *Appl. Surf. Sci.* **1988**, *33*, 811.
37. Díaz-Reyes, J.; Castillo-Ojeda, R.; Galván-Arellano, M.; Zaca-Moran, O. Characterization of WO₃ thin films grown on silicon by HFMOD. *Adv. Condens. Matter Phys.* **2013**, *2013*, 591787. [[CrossRef](#)]
38. Zhuo, R.F.; Feng, H.T.; Liang, Q.; Liu, J.Z.; Chen, J.T.; Yan, D.; Feng, J.J.; Li, H.J.; Cheng, S.; Geng, B.S.; et al. Morphology-controlled synthesis, growth mechanism, optical and microwave absorption properties of ZnO nanocombs. *J. Phys. D Appl. Phys.* **2008**, *41*, 185405. [[CrossRef](#)]

39. Zhang, R.; Yin, P.-G.; Wang, N.; Guo, L. Photoluminescence and Raman scattering of ZnO nanorods. *Solid State Sci.* **2009**, *11*, 865–869. [[CrossRef](#)]
40. Venkatesh, P.S.; Ramakrishnan, V.; Jeganathan, K. Raman silent modes in vertically aligned undoped ZnO nanorods. *Phys. B Condens. Matter* **2016**, *481*, 204–208. [[CrossRef](#)]
41. Souissi, A.; Marzouki, A.; Sayari, A.; Sallet, V.; Lusson, A.; Oueslati, M. Origin of the Raman mode at 379 cm⁻¹ observed in ZnO thin films grown on sapphire. *J. Raman Spectrosc.* **2011**, *42*, 1574–1577. [[CrossRef](#)]
42. Georgekutty, R.; Seery, M.K.; Pillai, S.C. A highly efficient Ag-ZnO photocatalyst: Synthesis, properties, and mechanism. *J. Phys. Chem. C* **2008**, *112*, 13563–13570. [[CrossRef](#)]
43. Decremps, F.; Pellicer-Porres, J.; Saitta, A.M.; Chervin, J.-C.; Polian, A. High-pressure Raman spectroscopy study of wurtzite ZnO. *Phys. Rev. B* **2002**, *65*, 092101. [[CrossRef](#)]
44. Khan, A. Raman Spectroscopic Study of the ZnO Nanostructures. *J. Pakistan Mater. Soc.* **2010**, *4*, 5–9.
45. Tayebi, M.; Tayyebi, A.; Masoumi, Z.; Lee, B.-K. Photocorrosion suppression and photoelectrochemical (PEC) enhancement of ZnO via hybridization with graphene nanosheets. *Appl. Surf. Sci.* **2019**, *502*, 144189. [[CrossRef](#)]
46. Liu, F.; Chen, X.; Xia, Q.; Tian, L.; Chen, X. Ultrathin tungsten oxide nanowires: Oleylamine assisted nonhydrolytic growth, oxygen vacancies and good photocatalytic properties. *RSC Adv.* **2015**, *5*, 77423–77428. [[CrossRef](#)]
47. Rettie, A.J.E.; Klavetter, K.C.; Lin, J.-F.; Dolocan, A.; Celio, H.; Ishiekwene, A.; Bolton, H.L.; Pearson, K.N.; Hahn, N.T.; Mullins, C.B. Improved visible light harvesting of WO₃ by incorporation of sulfur or iodine: A tale of two impurities. *Chem. Mater.* **2014**, *26*, 1670–1677. [[CrossRef](#)]
48. Thiyagarajan, T.; Deivasigamani, V.; Raj, M.; Joseph, C.; Dheivasigamani, T.; Palanivel, B.; Hamdy, M.S.; Shkir, M. Facile synthesis and characterization of WO₃/CuWO₄ nanocomposites for the removal of toxic methylene blue dye. *Korean J. Chem. Eng.* **2021**, *38*, 952–965. [[CrossRef](#)]
49. Ilican, S.; Caglar, M.; Aksoy, S.; Caglar, Y. XPS studies of electrodeposited grown f-doped ZnO rods and electrical properties of p-Si/n-FZN heterojunctions. *J. Nanomater.* **2016**, *2016*, 6729032. [[CrossRef](#)]
50. Limwichean, S.; Kasayapanand, N.; Ponchio, C.; Nakajima, H.; Patthanasettakul, V.; Eiamchai, P.; Meng, G.; Horprathum, M. Morphology-controlled fabrication of nanostructured WO₃ thin films by magnetron sputtering with glancing angle deposition for enhanced efficiency photo-electrochemical water splitting. *Ceram. Int.* **2021**, *47*, 34455–34462. [[CrossRef](#)]
51. Xu, S.; Fu, D.; Song, K.; Wang, L.; Yang, Z.; Yang, W.; Hou, H. One-dimensional WO₃/BiVO₄ heterojunction photoanodes for efficient photoelectrochemical water splitting. *Chem. Eng. J.* **2018**, *349*, 368–375. [[CrossRef](#)]
52. He, L.; Zhang, S.; Zhang, J.; Chen, G.; Meng, S.; Fan, Y.; Zheng, X.; Chen, S. Investigation on the mechanism and inner impetus of photogenerated charge transfer in WO₃/ZnO heterojunction photocatalysts. *J. Phys. Chem. C* **2020**, *124*, 27916–27929. [[CrossRef](#)]
53. Leonard, K.C.; Nam, K.M.; Lee, H.C.; Kang, S.H.; Park, H.S.; Bard, A.J. ZnWO₄/WO₃ composite for improving photoelectrochemical water oxidation. *J. Phys. Chem. C* **2013**, *117*, 15901–15910. [[CrossRef](#)]
54. Tahir, M.B.; Riaz, K.N.; Asiri, A.M. Boosting the performance of visible light-driven WO₃/g-C₃N₄ anchored with BiVO₄ nanoparticles for photocatalytic hydrogen evolution. *Int. J. Energy Res.* **2019**, *43*, 5747–5758. [[CrossRef](#)]
55. Othman, A.; Ali, M.A.; Ibrahim, E.; Osman, M. Influence of Cu doping on structural, morphological, photoluminescence, and electrical properties of ZnO nanostructures synthesized by ice-bath assisted sonochemical method. *J. Alloys Compd.* **2016**, *683*, 399–411. [[CrossRef](#)]
56. Saikia, L.; Bhuyan, D.; Saikia, M.; Malakar, B.; Dutta, D.K.; Sengupta, P. Photocatalytic performance of ZnO nanomaterials for self sensitized degradation of malachite green dye under solar light. *Appl. Catal. A Gen.* **2015**, *490*, 42–49. [[CrossRef](#)]
57. Othman, A.; Osman, M.; Ibrahim, E.; Ali, M.A. Sonochemically synthesized ZnO nanosheets and nanorods: Annealing temperature effects on the structure, and optical properties. *Ceram. Int.* **2016**, *43*, 527–533. [[CrossRef](#)]
58. Mazhdi, M.; Saydi, J.; Karimi, M.; Seidi, J.; Mazhdi, F. A study on optical, photoluminescence and thermoluminescence properties of ZnO and Mn doped-ZnO nanocrystalline particles. *Optik* **2013**, *124*, 4128–4133. [[CrossRef](#)]
59. Othman, A.; Osman, M.; Ibrahim, E.; Ali, M.A.; Abd-Elrahim, A. Mn-doped ZnO nanocrystals synthesized by sonochemical method: Structural, photoluminescence, and magnetic properties. *Mater. Sci. Eng. B* **2017**, *219*, 1–9. [[CrossRef](#)]
60. Zeng, H.; Duan, G.; Li, Y.; Yang, S.; Xu, X.; Cai, W. Blue luminescence of ZnO nanoparticles based on non-equilibrium processes: Defect origins and emission controls. *Adv. Funct. Mater.* **2010**, *20*, 561–572. [[CrossRef](#)]
61. Reddy, A.J.; Kokila, M.; Nagabhushana, H.; Chakradhar, R.; Shivakumara, C.; Rao, J.; Nagabhushana, B. Structural, optical and EPR studies on ZnO:Cu nanopowders prepared via low temperature solution combustion synthesis. *J. Alloys Compd.* **2011**, *509*, 5349–5355. [[CrossRef](#)]
62. Pancielejko, A.; Rzepnikowska, M.; Zaleska-Medynska, A.; Łuczak, J.; Mazierski, P. Enhanced visible light active WO₃ thin films toward air purification: Effect of the synthesis conditions. *Materials* **2020**, *13*, 3506. [[CrossRef](#)] [[PubMed](#)]
63. Hu, W.; Zhao, Y.; Liu, Z.; Dunnill, C.W.; Gregory, D.H.; Zhu, Y. Nanostructural Evolution: From One-Dimensional Tungsten Oxide Nanowires to Three-Dimensional Ferberite Flowers. *Chem. Mater.* **2008**, *20*, 5657–5665. [[CrossRef](#)]
64. Kato, K.; Uemura, Y.; Asakura, K.; Yamakata, A. Role of Oxygen Vacancy in the Photocarrier Dynamics of WO₃ Photocatalysts: The Case of Recombination Centers. *J. Phys. Chem. C* **2022**, *126*, 9257–9263. [[CrossRef](#)]
65. Szilágyi, I.M.; Fórizs, B.; Rosseler, O.; Szegedi, Á.; Németh, P.; Király, P.; Tárkányi, G.; Vajna, B.; Varga-Josepovits, K.; László, K.; et al. WO₃ photocatalysts: Influence of structure and composition. *J. Catal.* **2012**, *294*, 119–127. [[CrossRef](#)]

66. Ha, J.-H.; Muralidharan, P.; Kim, D.K. Hydrothermal synthesis and characterization of self-assembled h-WO₃ nanowires/nanorods using EDTA salts. *J. Alloys Compd.* **2009**, *475*, 446–451. [[CrossRef](#)]
67. Wang, M.; Kafizas, A.; Sathasivam, S.; Blunt, M.O.; Moss, B.; Gonzalez-Carrero, S.; Carmalt, C.J. ZnO/BiOI heterojunction photoanodes with enhanced photoelectrochemical water oxidation activity. *Appl. Catal. B Environ.* **2023**, *331*, 122657. [[CrossRef](#)]
68. Abd-Elrahim, A.; Chun, D.-M. Room-temperature deposition of ZnO-graphene nanocomposite hybrid photocatalysts for improved visible-light-driven degradation of methylene blue. *Ceram. Int.* **2021**, *47*, 12812–12825. [[CrossRef](#)]
69. Chen, H.M.; Chen, C.K.; Liu, R.-S.; Zhang, L.; Zhang, J.; Wilkinson, D.P. Nano-architecture and material designs for water splitting photoelectrodes. *Chem. Soc. Rev.* **2012**, *41*, 5654–5671. [[CrossRef](#)]
70. Jung, J.-Y.; Yu, J.-Y.; Lee, J.-H. Dynamic Photoelectrochemical Device with Open-Circuit Potential Insensitive to Thermodynamic Voltage Loss. *J. Phys. Chem. Lett.* **2018**, *9*, 5412–5418. [[CrossRef](#)]
71. Finger, F.; Welter, K.; Urbain, F.; Smirnov, V.; Kaiser, B.; Jaegermann, W. Photoelectrochemical Water Splitting using Adapted Silicon Based Multi-Junction Solar Cell Structures: Development of Solar Cells and Catalysts, Upscaling of Combined Photovoltaic-Electrochemical Devices and Performance Stability. *Z. Phys. Chem.* **2020**, *234*, 1055–1095. [[CrossRef](#)]
72. Guo, S.; Zhao, X.; Zhang, W.; Wang, W. Optimization of electrolyte to significantly improve photoelectrochemical water splitting performance of ZnO nanowire arrays. *Mater. Sci. Eng. B* **2018**, *227*, 129–135. [[CrossRef](#)]
73. Yagi, M.; Maruyama, S.; Sone, K.; Nagai, K.; Norimatsu, T. Preparation and photoelectrocatalytic activity of a nano-structured WO₃ platelet film. *J. Solid State Chem.* **2008**, *181*, 175–182. [[CrossRef](#)]
74. Liu, Y.; Li, Y.; Li, W.; Han, S.; Liu, C. Photoelectrochemical properties and photocatalytic activity of nitrogen-doped nanoporous WO₃ photoelectrodes under visible light. *Appl. Surf. Sci.* **2012**, *258*, 5038–5045. [[CrossRef](#)]
75. Li, W.; Li, J.; Wang, X.; Ma, J.; Chen, Q. Photoelectrochemical and physical properties of WO₃ films obtained by the polymeric precursor method. *Int. J. Hydrogen Energy* **2010**, *35*, 13137–13145. [[CrossRef](#)]
76. Gelderman, K.; Lee, L.; Donne, S.W.; Hermans, Y.; Klein, A.; Ellmer, K.; van de Krol, R.; Toupance, T.; Jaegermann, W.; Kang, H.-Y.; et al. Flat-band potential of a semiconductor: Using the Mott-Schottky equation. *J. Chem. Educ.* **2007**, *84*, 685–688. [[CrossRef](#)]
77. Schwarzburg, K.; Willig, F. Modeling of electrical transients in the semiconductor/electrolyte cell for photogeneration of charge carriers in the bulk. *J. Phys. Chem. B* **1997**, *101*, 2451–2458. [[CrossRef](#)]
78. Zhang, W.; Yan, D.; Appavoo, K.; Cen, J.; Wu, Q.; Orlov, A.; Sfeir, M.Y.; Liu, M. Unravelling Photocarrier Dynamics beyond the Space Charge Region for Photoelectrochemical Water Splitting. *Chem. Mater.* **2017**, *29*, 4036–4043. [[CrossRef](#)]
79. Ghorbani, M.; Abdizadeh, H.; Taheri, M.; Golobostanfard, M.R. Enhanced photoelectrochemical water splitting in hierarchical porous ZnO/Reduced graphene oxide nanocomposite synthesized by sol-gel method. *Int. J. Hydrogen Energy* **2018**, *43*, 7754–7763. [[CrossRef](#)]
80. Lv, R.; Wang, T.; Su, F.; Zhang, P.; Li, C.; Gong, J. Facile synthesis of ZnO nanopencil arrays for photoelectrochemical water splitting. *Nano Energy* **2014**, *7*, 143–150. [[CrossRef](#)]
81. Li, Y.; Liu, Z.; Wang, Y.; Liu, Z.; Han, J.; Ya, J. ZnO/CuInS₂ core/shell heterojunction nanoarray for photoelectrochemical water splitting. *Int. J. Hydrogen Energy* **2012**, *37*, 15029–15037. [[CrossRef](#)]

Disclaimer/Publisher's Note: The statements, opinions and data contained in all publications are solely those of the individual author(s) and contributor(s) and not of MDPI and/or the editor(s). MDPI and/or the editor(s) disclaim responsibility for any injury to people or property resulting from any ideas, methods, instructions or products referred to in the content.